University of Padova

Department of Physics and Astronomy "Galileo Galilei"

Master's Degree in Astrophysics and Cosmology

Master's thesis

Atmospheric Retrieval of the Hot Jupiter WASP-39b

Supervisor

Dr. Tiziano Zingales

University of Padova

Candidate

Ivan Stanković

Student ID: 2089815

Academic year

2023/2024

"There are three kinds of lies: lies, damned lies, and statistics."
— Mark Twain

Abstract

This thesis focuses on the atmospheric analysis of WASP-39b. I used Bayesian techniques to infer the main atmospheric parameters of this exoplanet, using a real transmission spectrum obtained by the NIRSpec instrument on board of the James Webb Space Telescope. The thesis integrates principles of spectral line formation, radiative transfer, and various absorption mechanisms, employing the TauREx and TauREx-2D retrieval frameworks alongside FastChem and the MultiNest sampler. A series of models of varying complexity were developed, ranging from one-dimensional isothermal models to two-dimensional models, with a set of different temperature-pressure profiles.

Model comparison is crucial to quantify the rationality of each physical assumption about the atmosphere and infer the most reasonable set of parameters to explaining the observed spectral features. The results suggest that one-dimensional models are adequate for this spectrum of WASP-39b, indicating no detectable day-night variations, with a difference of up to 20σ in favour of the 1D models. The models show evidence of a thermal inversion and a high mean molecular weight. The atmosphere is determined to be in chemical disequilibrium, as the tested free chemistry models have a greatly certain 20σ advantage to those with equilibrium chemistry. Likely detections of CO_2, H_2O, CO, H_2S, SO_2, Na, and K are consistent with existing studies, while the non-detections or weak detections of TiO, VO, and CH_4 are also noted. Further investigation is required to clarify the potential dissociation of H_2O and H_2 in the atmosphere.

Сажетак

Овај рад се бави атмосферском анализом вансоларне планете WASP-39b. Користећи бајесијанске методе, одређени су главни атмосферски параметри ове планете, користећи прави трансмисиони спектар снимљен NIRSPec инструментом који се налази на Џејмс Веб свемирском телескопу (JWST). Рад садржи детаљне описе принципа формирања спектралних линија, преноса зрачења и неколицине механизама апсорпције зрачења. Коришћени су TauREx и TauREx-2D програми за проналажење атмосферских параметара, уз FastChem за прорачуне са хемијском равнотежом и MultiNest за узорковање вредности параметара. Развијена је гарнитура атмосферских модела различитих сложености, од једнодимензионих изотермалних модела, до дводимензионих, са скупом различитих температурних профила.

Упоређивање модела је пресудно за одређивање рационалности сваке физичке претпоставке о атмосфери и за одређивање најразумнијег скупа апраметара за објашњење посматраних спектралних особина. Резултати указују да су једнодимензиони модели адекватни за овај спектар планете WASP-39b, што указује на недостатак мерљивих разлика између њене дневне и ноћне стране. Једнодимензиони модели имају статистичку предност од 20σ у поређењу са дводимензионим. Модели такође указују на постојање температурне инверзије, као и на високу средњу молекулску масу. Закључено је да је атмосфера ван хемијске равнотеже, пошто су модели са слободном хемијском конфигурацијом имали врло јаку статистичку предност од 20σ у односу на оне са хемијском равнотежом. Откривено присуство CO_2, H_2O, CO, H_2S, SO_2, Na и K је у складу са постојећим радовима, док је одсуство, или врло слаба заступљеност TiO, VO и CH_4 такође уочена. Потребна су додатна истраживања да разјасне могућу дисоцијацију H_2O и H_2 у овој атмосфери.

Contents

List of figures

List of tables

List of abbreviations

BOTS ..... Bright Object Time-Series
CIA ..... Collision-Induced Absorption
CSA ..... Canadian Space Agency
ESA ..... European Space Agency
FSs ..... Fixed Slits
FWHM ..... Full Width at Half-Maximum
GCM ..... Global Climate Model
HITRAN ..... HIgh-resolution TRANsmission molecular absorption database
HST ..... Hubble Space Telescope
IFU ..... Integral Field Unit
IR ..... Infrared
JWST ..... James Webb Space Telescope
LBL ..... Line-By-Line
LTE ..... Local Thermodynamic Equilibrium
MCMC ..... Markov Chain Monte Carlo
MIRI ..... Mid-Infrared Instrument
MOS ..... Multi-Object Spectroscopy
MSA ..... Micro-Shutter Assembly
NASA ..... National Aeronautics and Space Administration
NIRCam ..... Near Infrared Camera
NIRISS ..... Near Infrared Imager and Slitless Spectrograph
NIRSpec ..... Near Infrared Spectrograph
T-P ..... Temperature-Pressure
TauREx ..... Tau Retrieval for Exoplanets
TDPT ..... time-dependent perturbation theory
UV ..... Ultraviolet
WASP ..... Wide Angle Search for Planets
WFC3 ..... Wide Field Camera 3

1 Introduction

1.1 Exoplanet characterization

Since the first discovery of an exoplanet around a main sequence star (Mayor & Queloz 1995, [1]), the exoplanetary community has confirmed detections of more than 5700 exoplanets. The vast majority of these exoplanets were detected either using the radial velocity method, or the transit method. With radial velocity, one infers the (minimum) mass of the exoplanet, while with transits, one can infer the radius of an exoplanet. In rare cases both can be measured, giving us information about the planet's density - which can then give us a glimpse of the characteristics of the planet, its chemical composition and information about its formation.

High resolution spectroscopy of astronomical objects is possible with ground based instruments. In this way, one could also characterize the atmospheres of exoplanets. However, the issue of observing through the Earth's atmosphere exists, which limits the wavelength ranges in which observations could be feasible.

In Figure 1.1 it can be seen that the atmosphere of the Earth is highly absorbing at lower (UV, X-ray) and higher wavelengths (IR, microwave, and radio wavelengths, with the exception of a radio window) than those of visible light. For this reason it is crucial to also send telescopes to space, as they enable observations in the wavelength ranges which are not observable from the ground. This is also of great importance for exoplanetary atmospheric spectroscopy, as the bulk of these atmospheres has equilibrium temperatures which result in them having strong absorption in the infrared wavelength range.

With the launch of the Hubble Space Telescope (HST) opportunities started to arise for the characterization of the atmospheres of exoplanets. The atmospheric properties of tens of exoplanets were inferred, which gave a much more detailed understanding of both the chemical composition and the processes that occur on the planets. These opportunities have become even greater with the launch of the James Webb Space Telescope (JWST), which is both more sensitive and whose instruments have a broader spectral range. Because transiting exoplanets are the most numerous among those detected, transit spectroscopy is currently the core technique for the study

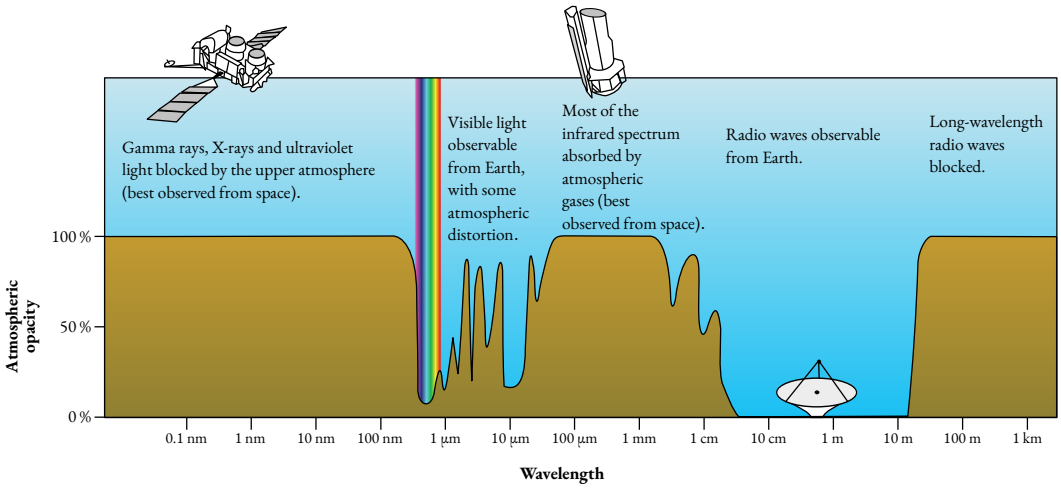

Figure 1.1: The opacity of the Earth's atmosphere. Image credit NASA.

of exoplanetary atmospheres.

One of the main goals of exoplanet science is the research of exoplanets in the habitable zones of their host stars. The characterization of the atmospheres of exoplanets is one of the ways in which this habitability could be possibly better defined and estimated [2], and this is why it is of great interest for the wider public, as well.

The current instruments used for transit spectroscopy enable insight into a vast range of new details about the atmospheres of exoplanets that have not been observable before, and that do not exist among the atmospheres of the planets in the Solar system. These include extremely high temperatures and pressures, large atmospheric sizes (inflated atmospheres), great temperature variations, day-night differences, greatly varying chemical compositions, different cloud coverage (uniform, inhomogeneous, or none) etc.

More detailed data provides an opportunity for a deeper understanding of the characteristics of exoplanets, but by revealing the influences of more physical processes on the observed radiation, it requires more complex models and therefore more computational power to analyze. This is why it is necessary to explore the limits to which less computationally expensive, simpler models are sufficient in explaining the observed phenomena, and to quantify the loss of precision when opting for these simpler models as opposed to more complex ones.

1.2 State of the art

This section provides a comprehensive review of research articles published on the exoplanet WASP-39b and its atmosphere, as well as on some similar exoplanets, to provide context on the current understanding we have about this and similar planets, as well as context on the methods used in said research. This will provide context on where the approach and results of this work stand within the broader domain of exoplanet atmosphere modelling.

WASP-39b was discovered in 2011 by Faedi et al. [3] within the Wide Angle Search for Planets (WASP) project.

WASP [4] is an international collaboration consisting of two ultra-wide angle telescopes covering the northern and southern hemispheres, surveying the entire sky and detecting exoplanets using transit photometry. After the discovery, a detailed transit follow-up was conducted and radial velocity observations were made, which constrained the planet's radius and mass, to establish it as a Jupiter-sized, Saturn-mass planet which is highly inflated; that is, its density is quite low.

Early transmission spectroscopy using HST's Wide-Field Camera 3 (WFC3), and the G102 and G141 spectroscopic grisms was performed on WASP-39b (Wakeford et al. 2018 [5]). This was done in the wavelength range between 0.8μm and 1.7μm. Using these observations, H_2O was detected in the atmosphere of this exoplanet with great certainty, and its atmospheric temperature and metallicity were established. This metallicity was unusually high. Spitzer spectroscopy was also performed.

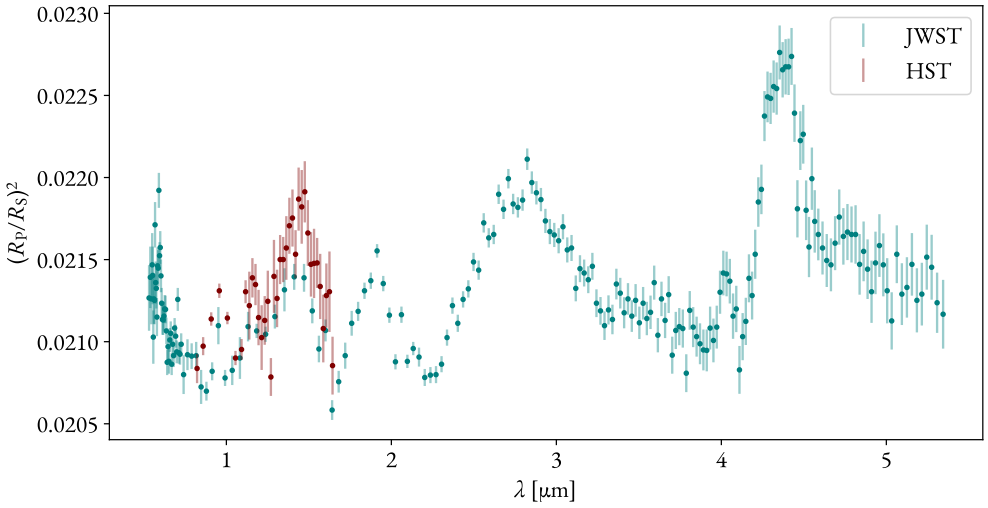

Figure 1.2: Comparison of a HST and JWST spectrum of WASP-39b. The Hubble spectrum (Wakeford et al. 2018 [5]) has a wavelength range between 0.8 and 1.7μm and enabled the detection of H_2O in the atmosphere of this exoplanet with a large certainty, while the JWST spectrum comprises wavelengths between 0.6 and 5.3μm, and enabled detections of several other molecules.

This planet was one of the first targets to be observed by the JWST after its launch. It was the first CO_2 detection outside of the Solar system (Ahrer et al. 2022 [6]). As part of the JWST Early Release Science program, a spectrum ranging from 0.5μm to 5.3μm was published by Rustamkulov et al. in 2023 [7]. Here, detections of CO_2, CO, H_2O, H_2S, SO_2 and Na were reported. Especially notable among these is SO_2, whose detection was slightly weaker than that of the other chemical species. It is the product of photochemical reactions, and would be the first detection of such a product in an exoplanetary atmosphere. The scale of improvement from a HST spectrum to a JWST spectrum can be seen in Figure 1.2.

The presence of SO_2 was further tested and confirmed with a suite of photochemical models by Tsai et al. in 2023 [8], and by additional Mid-InfraRed Instrument (MIRI) observations in 2024, by Powell et al. [9]. This also was in favour of an indication that WASP-39b is not in chemical equilibrium, which was suggested by Kawashima & Min in 2021 [10].

All of the previously mentioned spectral analyses modelled the atmosphere of WASP-39b as a one-dimensional one. However, as mentioned in the previous section, there is a strong possibility that three-dimensional features can be detected at the level of precision that is available with current instruments. Carone et al. in 2023 [11] created three-dimensional, Global Climate Models (GCMs) for WASP-39b. These models showed a patchy cloud composition, multiple possible solutions for the metallicity of the planet, and a relatively high S/O ratio. They also showed no thermal inversion in the temperature-pressure profiles of the planet, but showed a significant day-night difference in the temperature. This was further observationally checked by Espinoza et al. in 2024 [12], who found significant differences in the temperatures of the day and night terminators of the atmosphere of WASP-39b. Even greater day-night differences have been detected on WASP-43b also in 2024 by Bell et al. [13] using MIRI. This emphasizes the need for keeping these differences in mind when dealing with current exoplanetary transmission spectra.

There has also been work on other exoplanets that could be applied to WASP-39b as well. For example, TiO and VO have been detected as optical absorbers in hot Jupiters WASP-76b and WASP-121b by Tsiaras et al. 2018 [14], and should be probably looked out for in WASP-39b.

Another physical process that should be looked out for, as it was used to explain weaker spectral features in other hot Jupiters, is the dissociation of H_2O and H_2. This was explored through the example of WASP-121b by Parmentier et al. 2018 [15].

Considering the high estimates for the value of the mean molecular weight μ of WASP-39b, the work of Line & Parmentier from 2016 [16] should be considered, as they found a degeneracy between a patchy cloud coverage and a high μ in the way they manifest themselves in the total spectrum of an exoplanet - the spectra could be well explained by patchy clouds, without having the need for a large μ value. This was done with a theoretical approach on synthetic spectra, as well as real WFC3 spectra of HD189733b and HAT-P-11b.

Three-dimensional forward models of exoplanets are, however, very computationally expensive to make, and especially to perform retrievals with. For this reason, Falco et al. [17], Pluriel et al. [18] and Zingales et al. [19], all in 2022, created a tool for two-dimensional forward modelling and retrievals, as a compromise between the details of 3D models and the simplicity of 1D models, and performed tests to quantify the limits to which 2D effect would be observable.

Because of the previously mentioned high precision of the current instruments, namely JWST, all of the listed physical effects should be kept in mind when analyzing the atmosphere of WASP-39b. This work tries to take most of them into account, but using a relatively simplistic, computationally non-intensive approach.

1.3 Thesis structure

This work is split into several chapters. Each chapter has a summary at its beginning.

In this chapter I discussed the fundamentals of exoplanetary characterization, its importance, and made an overview of existing work on the exoplanet WASP-39b.
In **chapter 2** I will discuss the physics of the formation of spectra, with a focus on processes important for the spectra of exoplanets, and the fundamentals of radiative transfer, which is at the core of atmospheric modelling.
All the methods, statistical and software tools used in this work will be described in **chapter 3**.
The atmospheric models created will be presented and compared in **chapter 4**.
Chapter 5 is dedicated to the discussion of the main results, their comparison with the literature and the conclusions.

2

Theoretical background

In this chapter, I describe the principles of transmission spectroscopy (Section 2.1), as well as the physics of the main atmospheric processes (section 2.2) that, all together, contribute to the transmission spectrum of an exoplanet that can be observed (section 2.3).

Knowing how each of the processes influences the resulting spectrum allows us to do the opposite - by knowing only the spectrum of the exoplanet, we should be able to retrieve the parameters of the atmosphere that are responsible for its formation. These parameters include the temperature-pressure profile of the planet, the chemical species (absorbers) present and their volume mixing ratios, the scattering processes in the atmosphere, the presence or absence of clouds etc.

2.1 Transmission spectroscopy

Transmission spectroscopy is based on the fact that the depth (relative amount of stellar radiation blocked) of an exoplanetary transit - and therefore the apparent radius of the exoplanet - is wavelength dependent. This occurs because, during a transit, a fraction of the host star's light passes through the atmosphere which surrounds the planet [20]. If the atmosphere contains chemical species which are absorbing at certain wavelengths, more light will be blocked in those wavelengths, effectively increasing the measured radius of the planet. The same happens if some of the incident radiation at certain wavelengths is scattered (scattering and absorption together are usually referred to as extinction). Observing the transit at multiple wavelengths then results in a transmission spectrum (or transit spectrum). Emission spectroscopy, on the other hand, relies on the fact that the reduction in total radiation when the planet is eclipsed by the star is also wavelength dependent. This approach will not be the focus of this work.

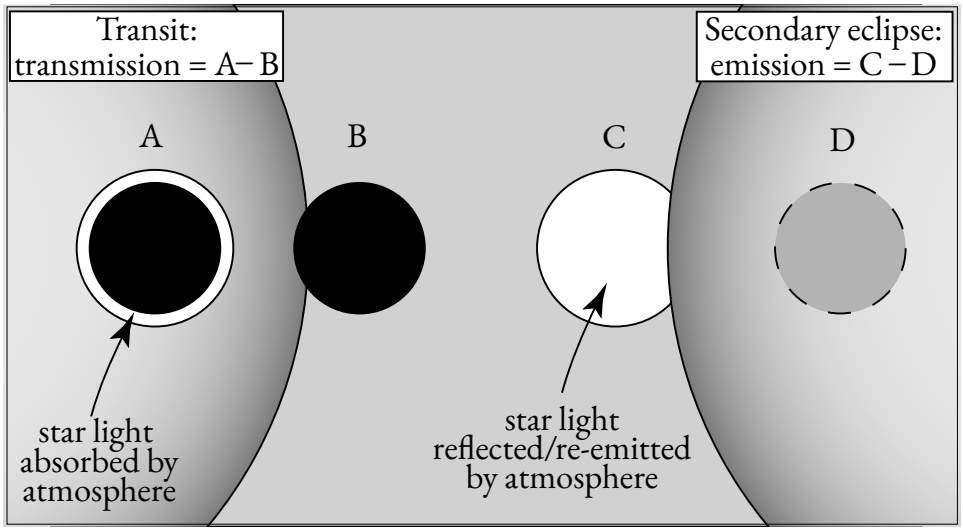

Figure 2.1: Geometry of transmission (left) and emission spectroscopy (right). During the transit, part of the background star light passes through the (annular) atmosphere of the planet. Adapted from *The Exoplanet Handbook*, 2nd edition (p. 284) [20], by M. A. C. Perryman, 2018, Cambridge University Press. Copyright Michael Perryman 2011, 2014, 2018.

As a first approximation, the magnitude of the transmission spectrum signal can be assumed to be the ratio of the atmospheric and host star surface areas. The area of the atmosphere, which is an annulus, is around $5H$ [21], where:

$$H = \frac{k_\mathrm{B} \cdot T}{\mu_m \cdot g_\mathrm{p}}, \tag{2.1}$$

H being the planetary scale height, k_B the Boltzmann constant, T the equilibrium temperature of the atmosphere, μ_m the mean molecular weight and g_p the planetary surface gravity. In terms of stellar ($R_\star$) and planetary (R_p) radii, a zeroth order estimate of the signal can be written as

$$\partial \simeq 5 \cdot \frac{2R_\mathrm{p}H}{R_\star^2}. \tag{2.2}$$

Based on Equations 2.1 and 2.2, it can be ascertained that the signature of an atmosphere is stronger for higher atmospheric temperatures, atmospheres composed of lighter elements and with lower gravities ($\partial \approx 10^{-4}$ for a Hot Jupiter with a H_2 dominated atmosphere). Considering the approximate maximum value of ∂ stated here, it can be expected that detecting atmospheres composed of heavier molecules (e.g. CO_2 atmospheres around rocky planets will be much more challenging to detect [21]).

In the following sections, I will describe more detailed models of the transit depth's dependence on wavelength, more in-depth models of the radiation transfer through the atmosphere, with regard to different absorption coefficients and mixing ratios of absorbing species, as well as taking into account other processes such as scattering and collision induced absorption.

2.1.1 Stellar radiation

The radiation of stars is also wavelength dependent, and this should be taken into account when measuring or modelling the transmission spectrum of an exoplanet's atmosphere. As a first approximation, the spectra of main sequence (therefore also Solar-type) stars can be modelled by a black body function, using Planck's law [22]:

$$B_\nu(\nu, T) = \frac{2h\nu^3}{c^2} \frac{1}{\exp\left(\frac{h\nu}{k_B T_e}\right) - 1}, \tag{2.3}$$

where B_ν is the spectral radiance of the body, h is Planck's constant, ν is the frequency of the emitted radiation, c is the speed of light, k_B is Boltzmann's constant, and T_e is the effective temperature of the emitting body. Most of the stellar radiation is, indeed, a continuum, but it also does exhibit absorption (in the visible and near-infrared) and emission (in the UV) lines. However, this has less of an impact in the wavelength ranges where the planetary atmospheres absorb the most radiation, which is deeper into the infrared range, because of the nature of the absorbing species (molecules) in the atmosphere of the exoplanet (to be elaborated in the following sections). Additionally, the spectral resolution of current space-based telescopes (e.g. HST/WFC3, Spitzer, JWST) which perform transit spectroscopy, is not high enough to resolve single spectral lines. For this reason as well, the stellar model does not meaningfully impact the atmospheric retrievals performed with low-resolution spectra. Therefore, a black body spectrum is usually considered a good enough approximation for the stellar radiation, when used for determining an atmospheric spectrum of an exoplanet around a main sequence quiet star.

2.2 Absorption in planetary atmospheres

As has been already affirmed, the absorption of stellar radiation by an exoplanetary atmosphere is wavelength dependent. To understand why this is so, we need to first look at how atoms and molecules interact with radiation (subsection 2.2.1). Then, molecular absorption with the respective molecular spectral lines will be explored, as these are the most significant in the atmospheres of exoplanets (subsection 2.2.2).

2.2.1 Spectral line formation

Bohr's model

To illustrate how absorption of photons by atoms works, one should look at one of the simplest models of absorption and emission line formation. Bohr (1913) postulated that the energy levels of an atom are quantized, and that the atoms can travel between these levels by absorbing and emitting radiation that corresponds to the energy difference between two levels:

$$E_k - E_j = h\nu, \tag{2.4}$$

where E_k is the energy of one (higher energy) state, E_j is the energy of another state, and ν is the frequency of an absorbed (if the atom moves from E_j to E_k) or emitted (if the atom moves from E_k to E_j) photon. There also exists a lowest possible energy state for the atoms, this being called the ground state. An atom in a state above the ground state is said to be in an excited state, and can return to the ground state by emitting a photon, as in Equation 2.4.

The different energy levels mentioned here are all so-called electronic levels, i.e. the electron of the atom moves between different states. This follows from Bohr's postulate that the angular momentum of the atom can take only discrete values. According to his model, the n-th energy level of a hydrogen atom can be expressed by:

$$E_n = -\frac{me^4}{8\varepsilon_0^2 h^2}\frac{1}{n^2}, \quad n = 1, 2, 3 \dots \tag{2.5}$$

where m is the mass of an electron, e the charge of an electron, ε_0 the permittivity constant, and n is the index of the discrete energy state. From here, the frequency of radiation required for a transition between any two states can be derived, if the selection rules permit. These selection rules are derived from the fact that Bohr postulated that the angular momentum can only have discrete values. The resulting spectrum in this case is composed of discrete spectral lines, each line corresponding to transition between certain energy state.

This, however, becomes much more complex for larger atoms with more electrons, and even more so for molecules, which are more likely to be active as absorbing species in an exoplanetary atmosphere, compared to hydrogen atoms. We will see, in the following subsection, that Bohr's solution for the hydrogen atom is really just the simplest solution of the more general Schrödinger wave equation, which (if solvable) yields solutions for stationary states for any atom or molecule.

Schrödinger wave equation

To fully understand why atoms and molecules have discrete energy states, and why the previously mentioned selection rules for transitions between these states exist, one must turn to the Schrödinger wave equation, which governs the behaviour of the wave function of a quantum-mechanical system (particle):

$$-i\hbar\frac{\partial\psi}{\partial t} = \frac{\hbar^2}{2m}\nabla^2\psi - E_p\psi, \tag{2.6}$$

ψ being the wave function, m the mass, and E_p the potential energy (which is time-independent). The Hamiltonian operator in this case is defined as:

$$H = -\frac{\hbar^2}{2m}\nabla^2 + E_p, \tag{2.7}$$

and using it Equation 2.6 can be rewritten as:

$$i\hbar\frac{\partial\psi}{\partial t} = H\psi. \tag{2.8}$$

It is possible to split the wave function ψ, which is position- and time-dependent , into two functions, one only dependent on position, and the other on time. This transforms Equation 2.8 into:

$$i\hbar\frac{1}{\varphi(t)}\frac{\mathrm{d}\varphi}{\mathrm{d}t} = \frac{1}{\phi(q)}H\phi(q), \tag{2.9}$$

$\varphi(t)$ being the time-dependent, and $\phi(q)$ being the time-independent part of the wave equation. Because the time-dependent and time-independent parts are separated in this equation, this means both sides have to be equal to the same constant. This constant has the dimension of energy, and is the total energy of the particle, denoted

with $-E$. This allows us to split Equation 2.9 into it's components:

$$\frac{\hbar^2}{2m}\nabla^2\phi + (E - E_p) = 0, \tag{2.10}$$

$$\frac{\mathrm{d}\varphi}{\mathrm{d}t} = \frac{1}{i\hbar}E\varphi. \tag{2.11}$$

The solution of Equation 2.11 (ignoring integration constants) is:

$$\varphi = \exp\left(\frac{Et}{i\hbar}\right), \tag{2.12}$$

so ψ can be written as:

$$\psi(q,t) = \phi(q)\exp\left(\frac{Et}{i\hbar}\right), \tag{2.13}$$

with the time-independent term $\phi(q)$ being constrained by Equation 2.10, and solvable only for some discrete values of E, these being the eigenvalues. This is the reason for the discreteness of energy levels of an atom or molecule. Inserting a Coulomb potential for E_p (an electron in the field of a proton) yields Bohr's solution (Equation 2.5) for the hydrogen atom. It should be noted that this approach is valid only for single-electron atoms. The Schrödinger equations becomes drastically more difficult to solve if the number of particles is more than one, and requires approximations to be solvable analytically, otherwise in most cases it will be solved numerically. In any case, the principle of the equation determining the energies of the different energy levels, regardless of the complexity of the system and the types of energy states (electronic, vibrational, rotational etc.) - all of them will be discrete.

Transitions and selection rules

The Schrödinger equation determines the energies of the individual discrete states of an atom or molecule. The wavefunctions that are the solutions of the equation are standing waves, and they determine the distribution of electronic charge that is time-independent [23]. To be able to transition from one state to another, the atom or molecule has to interact with electromagnetic radiation. This radiation creates an oscillating electric field:

$$\mathbf{E}(t) = |\mathbf{E}_0|\,\mathrm{Re}\left(\mathrm{e}^{-\mathrm{i}\omega t}\hat{\mathbf{e}}_{\mathrm{rad}}\right), \tag{2.14}$$

$|\mathbf{E}_0|$ being the (constant) amplitude, and $\hat{\mathbf{e}}_{\mathrm{rad}}$ being a unit vector which points in the direction of the oscillating field. If the electric field oscillation frequency ω lies close to the resonance frequency of the atom/molecule, it can push it into a superposition of two states and induce an electric dipole moment on the atom/molecule. To calculate stimulated transition probabilities and rates, one needs to approach this problem using time-dependent perturbation theory (TDPT). This is beyond the scope of this work. The result of these calculations gives Fermi's golden rule, which gives the rate of transitions:

$$\mathrm{Rate} \propto |e\mathbf{E}_0|^2 \left|\int \psi_2^*(\mathbf{r}\cdot\hat{\mathbf{e}}_{\mathrm{rad}})\psi_1 \mathrm{d}^3\mathbf{r}\right|^2 \equiv |e\mathbf{E}_0|^2 \times |\langle 2|\mathbf{r}\cdot\hat{\mathbf{e}}_{\mathrm{rad}}|1\rangle|^2, \tag{2.15}$$

with ψ_1 and ψ_2 being the wavefunctions of the two states between which the transition occurs (from 1 to 2). This equation basically states that the transition rate is proportional to the matrix element of the perturbation squared. Using spherical coordinates, the dipole matrix element can be written as:

$$\langle 2|\mathbf{r}\cdot\hat{\mathbf{e}}_{\text{rad}}|1\rangle = D_{12}\mathcal{I}_{\text{ang}}, \tag{2.16}$$

the radial integral being

$$D_{12} = \int_0^\infty R_{n_2,l_2}(r) r R_{n_1,l_1} r^2 \mathrm{d}r, \tag{2.17}$$

and the angular integral

$$\mathcal{I}_{\text{ang}} = \int_0^{2\pi}\int_0^{\pi} Y^*_{l_2,m_2}(\theta,\phi)\hat{\mathbf{r}}\cdot\hat{\mathbf{e}}_{\text{rad}} Y_{l_1,m_1}(\theta,\phi)\sin\theta \mathrm{d}\theta\mathrm{d}\phi. \tag{2.18}$$

with $\hat{\mathbf{r}} \equiv \frac{\mathbf{r}}{r}$, Y_{l_1,m_1} and Y_{l_2,m_2} being the eigenfunctions of the two states, and with $R_{n,l}$ denoting the radial wavefunction. A reminder is appropriate here that these equations apply to hydrogen-like atoms only, as the most simple case, which is used here to illustrate the principles that generally apply. The angular integral (Equation 2.18) is generally zero, unless strict criteria are satisfied. These criteria are known as selection rules. The selection rules stem from the conservation of angular momentum and parity.

All the stationary states of an atom or molecule can be described by a set of **quantum numbers** (the more complex the atom or molecule, the more combinations of quantum numbers it has). For the example of single-electron atoms, the wavefunction can be written as:

$$\Psi = |n\, l\, m_l\, s\, m_s\rangle\,, \tag{2.19}$$

with

$$n = 1, 2\ldots$$

being the principal quantum number (describes electron shells),

$$l = 0, 1, 2, \ldots, n-1$$

the azimuthal quantum number (describes subshells and gives the magnitude of the orbital angular momentum),

$$m_l = -l, -l+1, \ldots, l$$

the magnetic quantum number (gives the magnitude of the angular momentum projection along a specified axis), s the spin quantum number, being $s = \frac{1}{2}$ for electrons, and

$$m_s = -s, -s+1, \ldots, s$$

the magnetic spin quantum number, which for electrons can only be $m_s = -\frac{1}{2}$ or $\frac{1}{2}$.
Selection rules are generally expressed as a limitation on the values the various quantum numbers can have, as

shown on the example of hydrogen-like atoms here:

$$\Delta l = \pm 1; \quad \Delta m_l = 0, \pm 1; \quad \Delta s = 0; \quad \Delta m_s = 0.$$

The probability of any interaction, be it a transition, scattering, or the absorption of radiation by atoms or molecules, is usually expressed in terms of cross sections. Specifically, a cross section it quantifies how likely a photon of specific wavelength is to be absorbed by a specific particle. Physically, it denotes the amount of energy removed from the initial radiation beams by the particles the beam encounters its path towards the observer. The usual unit for cross sections is that of area [cm^2]. In the case of radiative transfer applications, it can be given as the mass extinction cross section [$cm^2 g^{-1}$], while if it is multiplied by particle number density [cm^{-3}] then it has units of inverse length [cm^{-1}] and is called the extinction coefficient. In infrared radiative transfer, the mass extinction cross section is just called the absorption coefficient [24].

Cross sections can be determined empirically or theoretically, although measuring them is preferred - considering the increasing complexity of the radiation-particle interaction equations with increasing particle size - while the theoretical approach is to be used if empirical measurements are impossible.

Line shapes

Energy states being discrete implies that the difference between them is very precisely constrained, and this would mean that the energy of a photon required for a transition to happen must be exactly the same - which would make spectral lines infinitely thin. In reality this is not the case. Several reasons for line width and mechanisms of line broadening exist, the principal being:

- natural line width,
- Doppler broadening,
- pressure broadening.

Natural line width originates from the uncertainty principle (Heisenberg 1927). Simply, with an excited state of a particle having energy E and lifetime t, and:

$$\Delta E \Delta t \geq \frac{\hbar}{2} \tag{2.20}$$

ΔE being the uncertainty in energy and Δt the uncertainty in the lifetime. Because of the finite lifetime of these states, the energy uncertainty, and therefore the frequency uncertainty of an absorbed/emitted profile - is finite. If atoms are approximated as dipoles, it can be shown that the shape of a naturally broadened line is that of a Lorentzian function. Nevertheless, the profile of the line is very narrow, in most cases too narrow to be detected in astrophysical spectra. The two other previously mentioned broadenings, however, are more significant and depend on the parameters of the medium from which the spectrum originates.

Doppler broadening of spectral lines exists because the particles, in any system, have non-zero velocities. If radiation of frequency $\nu_0$is absorbed by a particle moving with velocity v, the absorption frequency will be:

$$\nu = \nu_0 \left(1 \pm \frac{v}{c}\right), \tag{2.21}$$

for $v << c$. The particle velocities, in the case of thermodynamical equilibrium, will have the Maxwell-Boltzmann distribution:

$$f(v)\mathrm{d}v = \sqrt{\frac{m}{2\pi k_\mathrm{B} T}} \exp\left(-\frac{mv^2}{2k_\mathrm{B} T}\right)\mathrm{d}v, \tag{2.22}$$

m being the mass of an individual particle, T being the temperature of the system. Expressing v in terms of ν from Equation 2.21, the distribution becomes

$$f(\nu)\mathrm{d}\nu = \frac{1}{\sqrt{\pi}\alpha_D} \exp\left[-\left(\frac{\nu-\nu_0}{\alpha_D}\right)^2\right]\mathrm{d}\nu, \tag{2.23}$$

with

$$\alpha_D \equiv \nu_0 \sqrt{\frac{2k_\mathrm{B} T}{mc^2}}. \tag{2.24}$$

The absorption coefficient is

$$k_\nu^D = \frac{1}{\alpha_D \sqrt{\pi}} \exp\left[-\left(\frac{\nu-\nu_0}{\alpha_D}\right)^2\right]. \tag{2.25}$$

The function in Equation 2.23 is a Gaussian function, with α_D being its width - therefore it is a measure of the Doppler width of the spectral line. From Equation 2.23 the FWHM of the line is

$$\mathrm{FWHM}(\lambda) = 2\sqrt{\ln 2}\,\alpha_D. \tag{2.26}$$

Pressure broadening is a consequence of collisions between particles, which occur if particles are sufficiently close to each other. This is why it is also-called collisional broadening. The broadening is dependent on the pressure (or density) of the system, as well as on the temperature and therefore thermal velocity of the particles. The shape of a line broadened in this way is a Lorentz profile (Lorentz 1906):

$$k_\nu^p = \frac{1}{\pi} \frac{\alpha_p}{(\nu-\nu_0)^2 + \alpha_p^2}, \tag{2.27}$$

with α_p being the half-width at half-maximum. The dependence of α_p on temperature T and pressure p is, from the kinetic theory of gases:

$$\alpha_p = \alpha_0 \frac{p}{p_0} \left(\frac{T}{T_0}\right)^n, \tag{2.28}$$

α_0 being the value at $p_0 = 1013\mathrm{mbar}$ and $T_0 = 273\mathrm{K}$ [24], and n being dependent on the type of particle (molecule), ranging from $\frac{1}{2}$ to 1.

In the case where both pressure (Lorentzian line shape) and Doppler (Gaussian line shape) broadening are present, the two line profiles are convolved and form the so-called **Voigt profile**. If we denote the Doppler-broadened profile as $f_D(\nu-\nu')$ and the pressure broadened Lorentz profile as $f_p(\nu'-\nu_0)$, then the Voigt profile will be

$$f_V(\nu-\nu_0) = \int_{-\infty}^{+\infty} f_p(\nu'-\nu_0) f_D(\nu-\nu')\mathrm{d}\nu', \tag{2.29}$$

$$f_V(\nu - \nu_0) = \frac{1}{\pi^{\frac{3}{2}}} \frac{\alpha_p}{\alpha_D} \int_{-\infty}^{+\infty} \frac{1}{(\nu' - \nu_0)^2 + \alpha_p^2} \exp\left[- \left(\frac{\nu - \nu'}{\alpha_D} \right)^2 \right] \mathrm{d}\nu'. \tag{2.30}$$

Looking at the dependences of the Doppler and Lorentz profiles on frequency, it can be seen that the Doppler profile will dominate at the center of the line profile, while it will be much weaker at the wings of the line, where the Lorentz profile will dominate.

Other sources of line broadening can be the rotation of the observed body (star, planet) itself, as well as turbulence.

2.2.2 Molecular absorption lines

Molecules, being composed of multiple atoms connected by chemical bonds, not only can be in different electronic energy states (as atoms can), but can also be in different translational (unbound), vibrational - with respect to the interatomic bonds, and rotational states. In essence this means they have more ways of storing energy with respect to atoms. These vibrational and rotational states are quantized - similarly to the electronic states of atoms. Transitions between any of these states will involve absorption or emission of electromagnetic radiation. These transitions are not possible between every single combination of levels, rather the possible transitions are determined by selection rules.

To be able to interact with electromagnetic radiation, and therefore change from one energy state to another, the molecule must usually have an electric (or magnetic) dipole moment. This is commonly a result of asymmetric charge distributions for certain molecules (e.g. H_2O or O_3). These molecules have permanent electric dipole moments. Molecules that are linear, on the other hand, do not, but they do have weak magnetic dipole moments that enable them to be still be radiatively active.

Compared to electronic states, the the differences in energy between different vibrational and especially rotational states are much smaller. For electronic states, the order of magnitude is between 1eV and 10eV, for vibrational ones it is between 0.1eV and 1eV, while for rotational transitions it ranges from 0.001eV to 0.1eV. Vibrational transitions never occur on their own, but are in fact coupled with rotational transitions. These vibrational-rotational groups of lines lie in the intermediate-infrared spectrum, while purely rotational lines lie in the microwave and far-infrared range. Electronic lines, on the other hand, lie in the ultraviolet (UV) and visible spectrum.

In the same way the Schrödinger equation gives values for discrete electronic energy states, it does for vibrational-rotational ones. The approach in this case is that the Hamiltonian operator used is one for a harmonic oscillator (vibrations) rigid rotator (rotations). This Schrödinger equation is separable into its vibrational and rotational components. The solutions for rotational energy states are given by:

$$E_J = BhcJ(J+1), \tag{2.31}$$

J being the rotational quantum number, while the rotational constant B is given by

$$B = \frac{h}{8\pi^2 Ic}, \tag{2.32}$$

I being the moment of inertia of the molecule. Similarly, for vibrational states, we have

$$E_v = h\tilde{\nu}_k \left(v_k + \frac{1}{2} \right), \tag{2.33}$$

where $\tilde{\nu}_k$ is the fundamental vibrational frequency of the molecule, and v_k is the vibrational quantum number. The selection rules for rotational and vibrational transitions are

$$\Delta J = \pm 1, \ \Delta v_k = \pm 1,$$

with the exception of $\Delta v_k = -1$ being forbidden for transitions to and from $v_k = 0$, and $\Delta J = 0$ being permitted for certain vibrational modes. Because the vibration of molecules produces a significant enough electric dipole moment, it enables both vibrational and rotational transitions, and these two occur simultaneously. Considering that the vibrational energies are much larger than the rotational ones, rotational lines usually appear grouped around a certain vibrational line. The energies of these combined vibrational-rotational states are given by a simple sum of Equations 2.31 and 2.33:

$$E_{v,J} = BhcJ(J+1) + h\tilde{\nu}_k \left(v_k + \frac{1}{2} \right). \tag{2.34}$$

The frequencies of the lines produced by transitions between these states can be simply retrieved from Equation 2.4. It should be noted that all of the previous discussion has approximated molecules as harmonic oscillators and rigid rotators. In the more realistic, anharmonic case, all vibrational transitions are allowed, but the ones with $\Delta v = 0$ still remain the most probable.

Absorption by individual molecules

To understand how some specific of molecules absorb radiation, one must look into the structure of these molecules. The simplest molecules are composed of two atoms (diatomic molecules). Examples of these are N_2, O_2, CO, TiO and VO. If the molecules are composed of the same two atoms, they have a symmetric charge distribution and so no permanent electric dipole moment. These molecules are not active in the infrared and visible wavelength range. Diatomic molecules have a linear structure, and therefore can only vibrate along the axis that connects the two atoms. Because of this, they have only one vibrational mode v_1 - known as symmetric stretch.

Triatomic molecules (e.g. CO_2, SO_2, H_2O, O_3, H_2S etc.) can be divided into two categories: the first one comprises those with a linear symmetric configuration (CO_2), which do not have a permanent electric dipole moment, and the rest, which have a triangular structure and do have a permanent electric dipole moment. All of the triatomic molecules have three vibration modes - v_1 being symmetric stretch, v_2 bending and v_3 antisymmetric stretch. The difference is that the first mode of the molecules with linear symmetry is not radiatively active. CH_4 is an example of a five-atomic molecule, which has a symmetric structure (so no permanent dipole moment) and four vibration modes.

The number of rotational degrees of freedom of a molecule depends on its structure. For example, diatomic and linear triatomic molecules have two rotational degrees of freedom, and two equal moments of inertia. Asym-

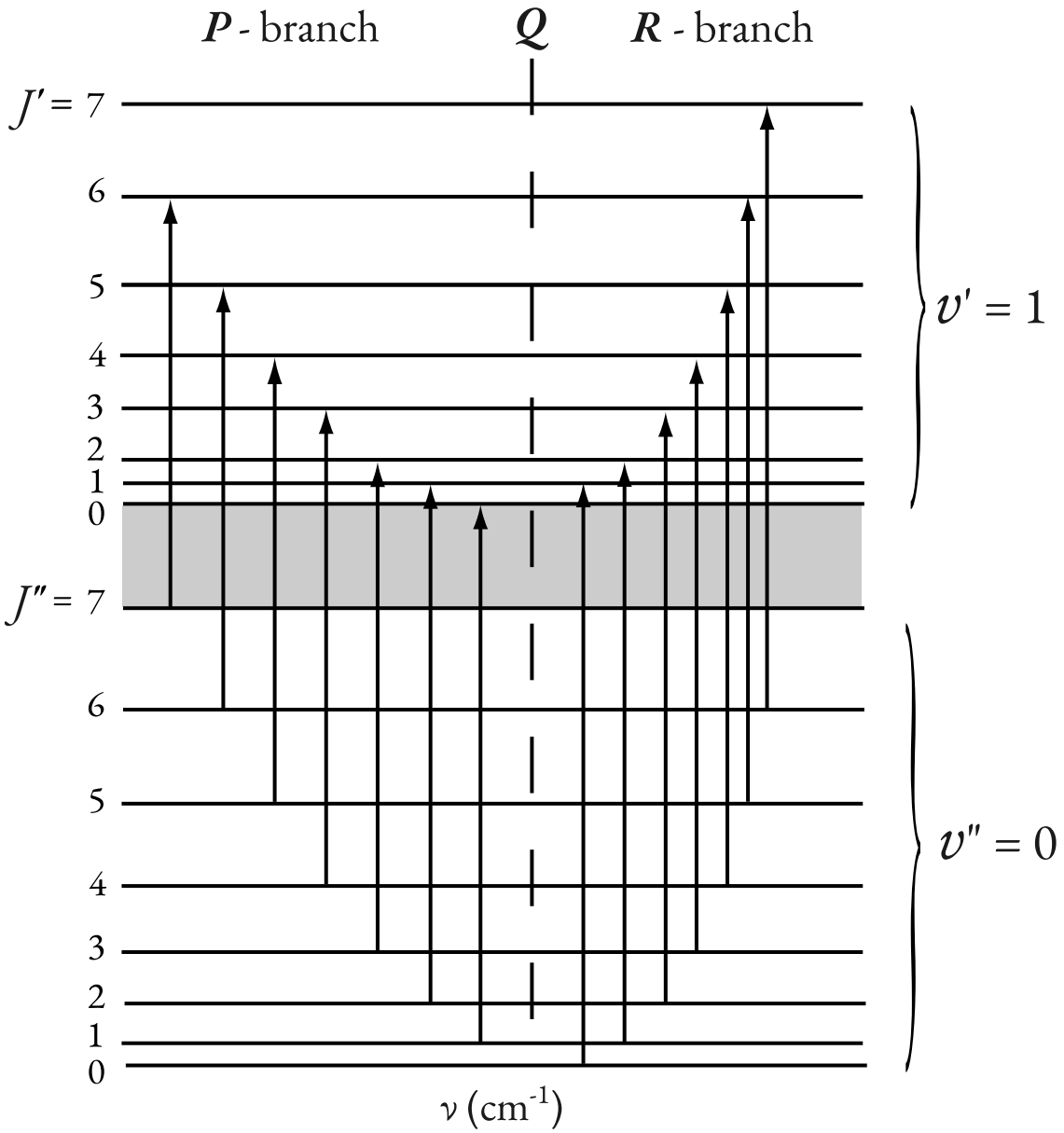

Figure 2.2: Simultaneous vibrational and rotational transitions. $\Delta J = 1$ produces the *P*-branch and $\Delta J = +1$ generates the *R*-branch. $\Delta J = 0$ shows the *Q*-branch that overlaps with the vibrational wavenumber. Adapted from *An Introduction to Atmospheric Radiation*, Second edition (Chapter 1, p. 19) [24], by K. N. Liou, 2002, Academic Press. Copyright 2002, 1980, Elsevier Science (USA).

metric triatomic molecules on the other hand have three unequal moments of inertia and three rotational degrees of freedom.

A lot of absorption processes for diatomic molecules are a combination of multiple types of transitions. This can frequently be a combination of electronic and vibrational transitions, that occur in the UV, visible and near-IR range. These two are usually connected because both electronic and vibrational energy derive from the elastic valence bonds that connect the two atoms. It should also be noted that molecules can undergo dissociation (splitting into their constituent atoms) in certain conditions, and this can decrease the absorption signature of the molecules while increasing that of the atoms.
Examples of species that have absorption bands in the UV are O_2, O_3, and N_2, while in the visible we have Na, TiO, and VO, and in the near-infrared CO_2, H_2O, CH_4, SO_2 and CO.

2.2.3 Collision-induced absorption

Another significant contributor to absorption is the mechanism of collision-induced absorption (CIA). The spectral contribution of CIA comes from interactions of multiple molecules and is called a supermolecular spectrum [25]. The atomic and molecular spectra which were the focus of the previous sections occur as a consequence of the internal dynamics of the atoms and molecules, while intermolecular interactions may just broaden or shift the spectral lines. Supermolecular spectra take into account the possibility of having interaction-induced dipole moments - that do not exist for individual molecules - and that can then themselves be a new source of spectral intensity, additional to the simple sum of the spectra of the individual atoms or molecules.

Collision-induced spectra usually arise from free-free transitions, i.e. transitions between unbound states (unlike pure molecular spectra which are usually a consequence of rotational-vibrational transitions). These states are not quantized, but are continuous. Individual molecules can, of course, have transitions between different translational states, but these are not radiatively active. Unlike them, the translational transitions of most "supermolecules" ("particles" that exist during the interaction between two or more molecules) are indeed radiatively active, the only exception being supermolecules that have a symmetry. These are usually pairs of identical (inert) atoms (He − He), while pairs of different atoms (He − Ar) or of identical molecules ($H_2 - H_2$) usually lack this symmetry. Exoplanets being mostly composed of molecular hydrogen and helium can therefore have CIA from $H_2 - H_2$ and $H_2 -$ He pairs.

The line profiles of collision-induced spectra are very broad, drawing simply from the Heisenberg uncertainty principle

$$\Delta\nu\Delta t \gtrsim \frac{1}{4\pi}, \tag{2.35}$$

because the durations Δt of the interactions between the molecules that form these lines are extremely short ($\Delta t \sim 10^{-12}$s). Usually, the energy of a photon absorbed by a non-reactive molecular pair will be spent on rotovibrational transitions in the individual molecules ($\Delta E_A, \Delta E_B$), as well as on the change in the energy of the relative motion of the molecules ΔE_{transl}, i.e:

$$h\nu = \Delta E_A + \Delta E_B + \Delta E_{\text{transl}}. \tag{2.36}$$

The line width will be given by the average E_{transl} which is of order $h\Delta\nu$ (following from Equation 2.35). If ΔE_A and ΔE_B are both zero, the line is a purely translational one, which occur in the far-infrared and microwave wavelength regions. However, if at least one of these is not zero, we will have collision-induced rotovibrational bands, whose

line centers are determined by the transition frequency of one of the individual molecules. These induced lines can be at frequencies of a non-induced allowed or forbidden line, and are much easier to measure at forbidden frequencies because of the lack of non-induced lines at these frequency ranges.
The line strenghts of induced dipoles are weaker than that of normal rotovibrational lines, because of the relative weakness of the induced dipoles.

It should be noted that every supermolecule has its own Hamiltionian and eigenfunctions - so if it is composed of N molecules it will have an N-particle Hamiltionian. In gases, however, the interactions are most frequently between pairs of molecules and can therefore be described by two-particle Hamiltonians - the only interaction that "matters" is that between the two molecules, and no other interaction influences them.

2.2.4 Scattering in planetary atmospheres

Apart from absorption, a significant amount of radiation is stopped from reaching the observer as a consequence of **scattering** - and therefore contributes to the total extinction that we measure as blocked stellar radiation. We have explored, in the previous section, the mechanisms of absorption of radiation, and in this section will expand on the physics of radiation scattering.

Rayleigh scattering [26]

In 1871 Lord Rayleigh described and discovered the simplest, but very significant mechanism of light scattering by particulates, which is named in his honor. Its principles can be examined on the example of sunlight scattering on air molecules in the Earth's atmosphere. Here we are considering a small spherical particle that is homogeneous and much smaller than the wavelength of the radiation it is interacting with. The radiation produces an electric field $\mathbf{E}_0$ (applied field) which induces an electric dipole moment $\mathbf{p}_0$ on the particle. Because of this induced dipole, the particle produces an electric field, which then interacts with the applied field in the vicinity of the particle and inside of it. We have:

$$\mathbf{p}_0 = \alpha \mathbf{E}_0, \tag{2.37}$$

where α is the polarizability of the particle. The induced electric dipole oscillates, and because of this it produces a plane-polarized electromagnetic wave - this is the scattered wave. Because the electric field of the scattered wave is quite complex close to the source, and because in the application of atmospheric spectroscopy it will be observed from afar, we will consider it in the far-field approximation.

$$\mathbf{E} = \frac{1}{c^2}\frac{1}{r}\frac{\partial^2 \mathbf{p}}{\partial t^2}\sin\gamma, \tag{2.38}$$

where $\mathbf{E}$ is the scattered field, r the distance between the dipole and observer, $\mathbf{p}$ is the scattered dipole moment, and γ is the angle between the scattered dipole moment and the direction of observation. If the field is periodically oscilating, the scattered dipole moment is related to the induced one as:

$$\mathbf{p} = \mathbf{p}_0 e^{-ik(r-ct)}, \tag{2.39}$$

with $k = \frac{2\pi\nu}{c}$ being the wavenumber. If this is inserted into Equation 2.38 we get:

$$\mathbf{E} = -\mathbf{E}_0 \frac{e^{-ik(r-ct)}}{r} k^2 \alpha \sin\gamma. \tag{2.40}$$

Because solar radiation (and generally stellar radiation) is unpolarized, the electric field of its radiation can be split into any two perpendicular and identical vectors, which will here be chosen to be perpendicular and parallel to the plane of scattering, and will be labeled as E_{0r} and E_{0l} respectively. The particles on which the scattering occurs (atmospheric molecules) will be the same as previously approximated. Therefore

$$E_r = -E_{0r} \frac{e^{-ik(r-ct)}}{r} k^2 \alpha \sin\gamma_1, \tag{2.41a}$$

$$E_l = -E_{0l} \frac{e^{-ik(r-ct)}}{r} k^2 \alpha \sin\gamma_2, \tag{2.41b}$$

with $\gamma_1 = \frac{\pi}{2}$ always because the scattered dipole moment in the r direction is always perpendicular to the scattering plane, and $\gamma_2 = \gamma_1 - \Theta$, with Θ being the scattering angle, i.e. the angle between the incident and scattered wave. Transforming the electric fields into intensities using $I_0 = C|E_0|^2$ and analogously for I, with C being a proportionality factor such that C/r^2 is a solid angle. We get

$$I_r = I_{0r} \frac{k^4 \alpha^2}{r^2}, \tag{2.42a}$$

$$I_l = I_{0l} \frac{k^4 \alpha^2 \cos\Theta}{r^2}, \tag{2.42b}$$

I_r and I_l being the polarized intensities that are perpendicular and parallel, respectively, to the plane of scattering. From here we can get the total scattered intensity:

$$I = I_r + I_l = \frac{I_0}{r^2} \alpha^2 \left(\frac{2\pi}{\lambda}\right)^4 \frac{1+\cos^2\Theta}{2}, \tag{2.43}$$

considering $I_{0r} = I_{0l} = I_0/2$ for unpolarized sunlight (starlight), and λ being the wavelength of the radiation. This is the scattering equation derived by Rayleigh, and most notably it shows how the scattered is inversely proportional to λ^4, which means that shorter wavelength radiation is much more prone to scattering.

Angular distribution and cross section of scattered energy

We define a non-dimensional phase function $P(\cos\Theta)$, such that

$$\int_0^{2\pi} \int_0^{\pi} \frac{P(\cos\Theta)}{4\pi} \sin\Theta \mathrm{d}\Theta \mathrm{d}\phi = 1. \tag{2.44}$$

The phase function for the case of Rayleigh scattering of unpolarized starlight is

$$P(\cos\Theta) = \frac{3}{4}(1+\cos^2\Theta). \tag{2.45}$$

Using this, Equation 2.43 can be rewritten as

$$I(\Theta) = \frac{I_0}{r^2}\alpha^2\frac{128\pi^5}{3\lambda^4}\frac{P(\Theta)}{4\pi}. \tag{2.46}$$

To find the scattered flux f, the scattered flux density ($I\Delta\Omega$) needs to be integrated over a certain area whose distance from the scatterer is r:

$$f = \int_\Omega (I\Delta\Omega)r^2 \mathrm{d}\Omega, \tag{2.47}$$

$r^2\mathrm{d}\Omega$ being the infinitesimal area and $\mathrm{d}\Omega$ being an infinitesimal solid angle. Integrating this over a sphere and defining the incident flux as $F_0 = I_0\Delta\Omega$, we have

$$f = F_0\alpha^2\frac{128\pi^5}{3\lambda^4}, \tag{2.48}$$

which then allows us to define the scattering cross section per molecule as

$$\sigma_s = \frac{f}{F_0} = \alpha^2\frac{128\pi^5}{3\lambda^4}. \tag{2.49}$$

This cross section is dimensionally area, and represents the amount of incident radiation removed by a single scattering event. This also allows us to rewrite Equation 2.46 as

$$I(\Theta) = I_0\frac{\sigma_s}{r^2}\frac{P(\Theta)}{4\pi}. \tag{2.50}$$

Previously, the polarizability α was mentioned without elaborating on this parameter. It originates from the principle of dispersion of electromagnetic waves

$$\alpha = \frac{3}{4\pi N_s}\left(\frac{m^2-1}{m^2+2}\right), \tag{2.51}$$

N_s being the total number of molecules per unit volume and m is the molecular refractive index. Generally, m is composed of a real m_r and imaginary m_i part, which correspond respectively to the scattering and absorption properties of the atoms and molecules of the medium through which the radiation is passing.
In an atmosphere that is scattering dominated, the optical depth at a given wavelength can be defined:

$$\tau(\lambda) = \sigma_s(\lambda)\int_0^{z_\infty} N(z)\mathrm{d}z, \tag{2.52}$$

where $N(z)$ is the number density of particles as a function of height, with z_∞ denoting the top of the atmosphere. The concept of optical depth will be further elaborated upon, including both scattering and absorption, in section 2.3.

The size of scattering particles can be parametrized with the so-called size parameter x:

$$x = \frac{2\pi a}{\lambda}, \tag{2.53}$$

a being the particle's radius and λ the wavelength of the radiation being scattered. In this subsection we explored Rayleigh scattering, which occurs for $x \ll 1$.

Lorenz-Mie scattering

If particles are of such size that $x \gtrsim 1$, the scattering mechanism is referred to as Lorenz-Mie scattering. Generally, as in Equation 2.50, the scattered intensity is given by:

$$I(\Theta) = I_0 \left(\frac{\sigma_s}{r^2}\right) \frac{P(\Theta)}{4\pi},$$

where σ_s is the scattering cross section, that will be different for different kinds of scattering, and all other quantities have been defined previously (see Equation 2.50). From the Lorenz-Mie theory of scattering by spheres, the scattering efficiency Q_s can be written as

$$Q_s = \frac{\sigma_s}{\pi a^2} = c_1 x^4 (1 + c_2 x^2 + c_3 x^4 + \dots), \tag{2.54}$$

where x has been defined in Equation 2.53 and the coefficients are

$$c_1 = \frac{8}{3}\left(\frac{m^2-1}{m^2+2}\right)^2, \tag{2.55}$$

$$c_2 = \frac{6}{5}\left(\frac{m^2-1}{m^2+2}\right), \tag{2.56}$$

$$c_3 = \frac{3}{175}\frac{m^6 + 41m^4 - 28m^2 + 284}{(m^2+2)^2} + \frac{1}{900}\left(\frac{m^2+2}{2m^2+2}\right)^2 \left[15 + (2m^2+3)^2\right]. \tag{2.57}$$

The term of c_1 dominates for small particles (molecules), so for Rayleigh scattering the other terms can be neglected, so the scattering intensity is inversely proportional to λ^4. For larger particles (aerosols, clouds), the other terms cannot be neglected and scattering will be less dependent on wavelength, and mostly dependent on particle size.

The phase function $P(\Theta)$ can also be calculated from the Lorenz-Mie theory for spheres - the results of this theory (also the ones presented here), require derivations beginning from Maxwell's equations, but for the scope of this work, this qualitative description should suffice.

It should be also finally noted, that for even larger particles (i.e. particles much larger than the incident wavelength), the radiation blocked is based purely on (geometric) reflection and refraction, so the extinction cross section σ_e for these processes is equivalent to double the geometric area A of the particles

$$\sigma_e = 2A. \tag{2.58}$$

If the particle in question is nonabsorbing, then $\sigma_e = \sigma_s$.

2.3 Radiative transfer

As has been demonstrated in the previous sections, incoming stellar radiation can be significantly blocked and/or changed along its path through a medium, before reaching an observer. We have explored the physics of the absorption (section 2.2) of radiation and of radiation scattering (subsection 2.2.4). To be able to understand how all of these processes together change and influence the incident radiation, one must take a look at the principles of **radiative transfer**.

The reduction of intensity of a radiation beam $\mathrm{d}I_\lambda^-$ when passing through a layer of thickness $\mathrm{d}s$ is

$$\mathrm{d}I_\lambda^- = k_\lambda \rho I_\lambda \mathrm{d}s, \tag{2.59}$$

where I_λ is the radiation intensity before entering the medium, k_λ the mass extinction (comprising both absorption and scattering) cross section and ρ is the density of the medium, while λ is the wavelength of the radiation. The radiation beam can, of course, be strengthened by emission from the medium, so the enhancement of intensity from the same layer will be

$$\mathrm{d}I_\lambda^+ = j_\lambda \rho \mathrm{d}s, \tag{2.60}$$

with j_λ being the source function coefficient and having the same dimensions as k_λ. Therefore the total change of intensity will be

$$\mathrm{d}I_\lambda = -k_\lambda \rho I_\lambda \mathrm{d}s + j_\lambda \rho \mathrm{d}s, \tag{2.61}$$

and with the definition of the source function $J_\lambda \equiv j_\lambda / k_\lambda$ this can be rewritten as

$$\frac{\mathrm{d}I_\lambda}{k_\lambda \rho \mathrm{d}s} = -I_\lambda + J_\lambda. \tag{2.62}$$

This is the general equation of radiative transfer, independent of the coordinate system chosen.

2.3.1 Non-emitting medium

If emission from the atmosphere can be neglected, along with multiple scattering (which is true, for example, for solar radiation transfer through the atmosphere of the Earth, in visible wavelengths), then the Equation 2.62 reduces to:

$$\frac{\mathrm{d}I_\lambda}{k_\lambda \rho \mathrm{d}s} = -I_\lambda. \tag{2.63}$$

If the incident intensity (at $s = 0$) is $I_\lambda(0)$, then the outgoing intensity will be, by integrating the previous equation

$$I_\lambda(s_1) = I_\lambda(0) \exp\left(- \int_0^{s_1} k_\lambda \rho \mathrm{d}s \right). \tag{2.64}$$

If k_λ is independent of s, then the path length can be defined

$$u = \int_0^{s_1} \rho \mathrm{d}s, \tag{2.65}$$

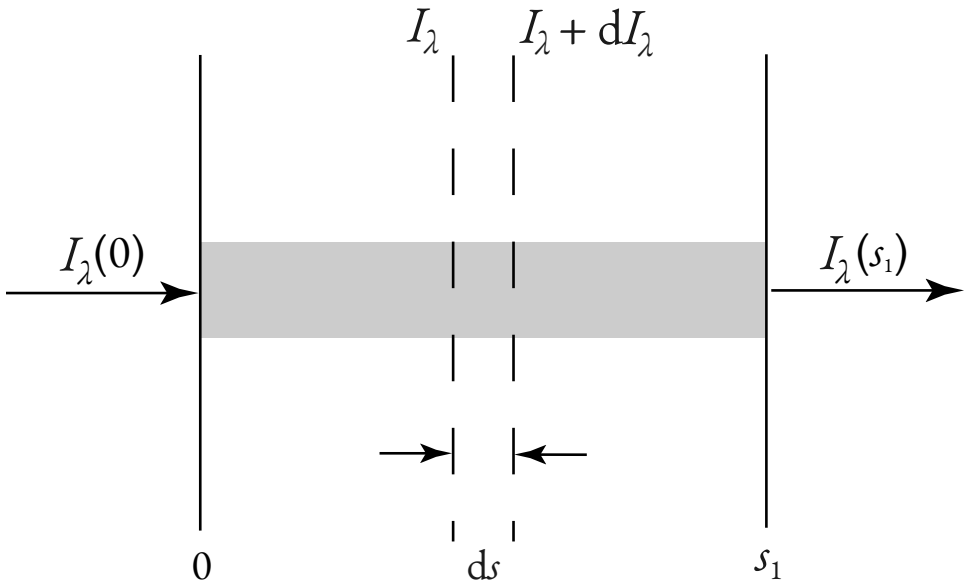

Figure 2.3: Depletion of the radiant intensity in traversing an extinction medium. Adapted from *An Introduction to Atmospheric Radiation*, Second edition (Chapter 1, p. 28) [24], by K. N. Liou, 2002, Academic Press. Copyright 2002, 1980, Elsevier Science (USA).

which together with Equation 2.64 gives

$$I_\lambda(s_1) = I_\lambda(0)e^{-k_\lambda u}, \tag{2.66}$$

the Beer-Bougert-Lambert law. This gives the reduction in intensity of a radiation beam travelling through a homogeneous medium. It is also applicable to the flux.

A few new quantities can be defined here. Firstly, the transmisivity at a certain wavelength:

$$T_\lambda = \frac{I_\lambda(s_1)}{I_\lambda(0)} = e^{-k_\lambda u}, \tag{2.67}$$

and consequently, the absorptivity

$$A_\lambda = 1 - T_\lambda = 1 - e^{-k_\lambda u}. \tag{2.68}$$

Also, if there is both absorption and scattering, a portion of the radiation will be reflected away (backscattered), so the reflectivity can be defined from

$$T_\lambda + A_\lambda + R_\lambda = 1, \tag{2.69}$$

and, in this way, all of the ways incident radiation can be redirected are taken account for.

2.3.2 Non-scattering, LTE medium

It is useful to analyze another simple case - one with no scattering and of a medium in local thermodynamic equilibrium (which is applicable to the case of emitted infrared radiation of a planet passing through its atmosphere). The source function in this case will be the Planck function (Equation 2.3).

$$J_\lambda = B_\lambda(T), \tag{2.70}$$

and Equation 2.62 becomes

$$\frac{\mathrm{d}I_\lambda}{k_\lambda \rho \mathrm{d}s} = -I_\lambda + B_\lambda(T), \tag{2.71}$$

and k_λ is now the absorption coefficient, since there is no scattering. Here it proves convenient to define the monochromatic optical thickness (depth) between two points s and s_1 in the medium on the path of the radiation beam:

$$\tau_\lambda(s_1, s) \equiv \int_s^{s_1} k_\lambda \rho \mathrm{d}s', \tag{2.72}$$

with

$$\mathrm{d}\tau_\lambda(s_1, s) = -k_\lambda \rho \mathrm{d}s. \tag{2.73}$$

This enables us to transform Equation 2.71 into

$$-\frac{\mathrm{d}I_\lambda(s)}{\mathrm{d}\tau_\lambda(s_1, s)} = -I_\lambda(s) + B_\lambda[T(s)], \tag{2.74}$$

which can be solved by multiplying with $e^{-\tau_\lambda(s1,s)}$ and then integrating over ds from 0 to s_1, to give

$$I_\lambda(s_1) = I_\lambda(0)e^{-\tau_\lambda(s_1,0)} + \int_0^{s_1} B_\lambda[T(s)]e^{-\tau_\lambda(s1,s)} k_\lambda \rho \mathrm{d}s. \tag{2.75}$$

This equation is called the Schwarzschild equation.

2.3.3 Plane-parallel atmosphere approximation

Geometrically, the simplest approximation for analyzing the transfer of radiation through atmospheric layers, is that of a plane-parallel atmosphere. This is applicable if the layer of the atmosphere through which the radiation passes is much smaller than the radius of the planet, and also if the atmospheric parameters only vary in one dimension, i.e. they only change with height. It is therefore appropriate to set up a coordinate system in the direction of these changes, which is normal to the plane of stratification. If the distance in this direction is denoted by z, then Equation 2.62 becomes

$$\mu \frac{\mathrm{d}I_\lambda(z, \theta, \phi)}{k_\lambda \rho \mathrm{d}z} = -I_\lambda(z, \theta, \phi) + J_\lambda(z, \theta, \phi), \tag{2.76}$$

where θ is the angle between the radiation beam and the z direction (upward), and ϕ is the azimuthal angle with regard to the x-axis, and $\mu = \cos\theta$ Here, we can again define the optical thickness τ:

$$\tau_\lambda = \int_z^\infty k_\lambda \rho \mathrm{d}z', \tag{2.77}$$

so Equation 2.76 becomes

$$\frac{\mathrm{d}I_\lambda(\tau_\lambda, \theta, \phi)}{\mathrm{d}\tau_\lambda} = I_\lambda(\tau_\lambda, \theta, \phi) - J(\tau_\lambda, \theta, \phi). \tag{2.78}$$

This equation can be solved similarly to the Equation 2.74, yielding solutions for the upward and downward intensities, in an atmosphere bounded by $\tau_\lambda = 0$ and $_\lambda = \tau_*$, these being, respectively

$$I_\lambda(\tau_\lambda, \mu, \phi) = I_\lambda(\tau_*, \mu, \phi) e^{-\frac{\tau_* - \tau_\lambda}{\mu}} + \int_{\tau_\lambda}^{\tau_*} J(\tau_\lambda', \mu, \phi) e^{-\frac{\tau_\lambda' - \tau_\lambda}{\mu}} \frac{\mathrm{d}\tau_\lambda'}{\mu}, \tag{2.79}$$

and

$$I_\lambda(\tau_\lambda, -\mu, \phi) = I_\lambda(0, -\mu, \phi) e^{-\frac{\tau_\lambda}{\mu}} + \int_0^{\tau_\lambda} J(\tau_\lambda', -\mu, \phi) e^{-\frac{\tau_\lambda - \tau_\lambda'}{\mu}} \frac{\mathrm{d}\tau_\lambda'}{\mu}, \tag{2.80}$$

the upward solution corresponding to $\mu > 0$ and the downward one corresponding to $\mu < 0$. The first terms on the right of these two equations are the incident source intensities at the bottom and top layers. For observational purposes, the outward intensities are needed. These can be obtained by setting $\tau_\lambda = 0$ in Equation 2.79 and $\tau_\lambda = \tau_*$ in Equation 2.80, to obtain, respectively:

$$I_\lambda(0, \mu, \phi) = I_\lambda(\tau_*, \mu, \phi) e^{-\frac{\tau_*}{\mu}} + \int_{\tau_\lambda}^{\tau_*} J(\tau_\lambda', \mu, \phi) e^{-\frac{\tau_\lambda'}{\mu}} \frac{\mathrm{d}\tau_\lambda'}{\mu}, \tag{2.81}$$

which represents the top surface contribution, attenuated at the bottom, and

$$I_\lambda(\tau_*, -\mu, \phi) = I_\lambda(0, -\mu, \phi) e^{-\frac{\tau_*}{\mu}} + \int_{\tau_\lambda}^{\tau_*} J(\tau_\lambda', -\mu, \phi) e^{-\frac{\tau_* - \tau_\lambda'}{\mu}} \frac{\mathrm{d}\tau_\lambda'}{\mu}, \tag{2.82}$$

which represents the internal atmospheric contribution.

2.3.4 Absorption by specific chemical species

For the consideration of a simple atmosphere, like in the previous subsections (non-scattering with plane-parallel geometry), the monochromatic optical depth originating from a single absorber can be written as

$$\tau_\lambda(z) = \int_z^\infty n(z) \sigma_a \mathrm{d}z, \tag{2.83}$$

with $n[\mathrm{cm}^{-3}]$ being the number density of the absorber, and $\sigma_a[\mathrm{cm}^2]$ being the absorption cross section of said absorber. The flux, with regard to the intensity, can be defined as

$$F(z) = \int_0^{2\pi} \int_{-1}^{1} I(z, \mu, \phi) \mu \mathrm{d}\mu \mathrm{d}\phi. \tag{2.84}$$

The reduction of stellar flux entering at a zenith angle θ_0 will then be

$$F(z) = \mu_0 F_0 e^{-\frac{\tau_\lambda(z)}{\mu_0}}, \tag{2.85}$$

with F_0 being the incident flux and $\mu_0 = \cos\theta_0$.

The concentration of an absorbing species can, for example, vary exponentially with height, according to a scale height

$$n(z) = n_0 e^{-\frac{z}{H}}, \tag{2.86}$$

n_0 being the concentration at $z = 0$ and H being the scale height. The volume absorption rate $q(z)[\mathrm{cm}^{-3}\mathrm{s}^{-1}]$ can be defined as

$$q(z) = \frac{\mathrm{d}F(z)}{\mathrm{d}z/\mu_0} = F_0 n(z)\sigma_a e^{-\frac{\tau_\lambda}{\mu_0}}, \tag{2.87}$$

and can be rewritten using Equation 2.84 and Equation 2.86 as

$$q(z) = F_0\sigma_a n_0 \exp\left(-\frac{z}{H} - \frac{1}{\mu_0}\sigma_a n_0 e^{-\frac{z}{H}}\right). \tag{2.88}$$

Usually, there is more than one absorber in an atmosphere. So far the equations described the attenuation of radiation in the case of a single absorbing species. To take into account multiple absorbing species, one simply sums the optical depths that stem from each of them:

$$\tau_\lambda(z) = \sum_i \int_z^\infty n_i(z)\sigma_a(n_i,\lambda)\mathrm{d}z, \tag{2.89}$$

where the index i denotes the individual absorbers.

To more closely analyze absorption, and understand the meaning of the spectral absorptivity mentioned in Equation 2.68, one should look to its definition:

$$A_{\hat{\lambda}}(\tau_{\hat{\lambda}}) = \int_{\Delta\lambda}\left(1 - e^{-\frac{\tau_\lambda}{\mu_0}}\right)\frac{\mathrm{d}\lambda}{\Delta\lambda} \tag{2.90}$$

where $\Delta\lambda$ is the spectral interval for which the specific absorptivity is defined. In the case this interval is small and the stellar flux weakly varies in it, then the attenuated flux can be written using the absorptivity as

$$F_{\hat{\lambda}}(z) \simeq \mu_0 F_0(\hat{\lambda})[1 - A_{\hat{\lambda}}(\tau_{\hat{\lambda}})]. \tag{2.91}$$

Techniques for calculating the absorptivity will be elaborated upon in some of the following sections.

2.3.5 Atmosphere with scattering and absorption

In the previous subsections an atmosphere that is non-scattering and plane parallel was considered. In reality, however, both scattering and absorption are present, so in this subsection a more realistic atmosphere that is both scattering and absorbing will be examined.

The extinction, scattering and absorption coefficients for a layer of thickness Δz can be defined with

$$\beta_{e,s,a} = \int_{\Delta z} \sigma_{e,s,a}(z) n(z) \frac{\mathrm{d}z}{\Delta z}, \tag{2.92}$$

where $\sigma(z)$ are cross sections for the processes and $n(z)$ is the number density. If we denote the phase function as $P(\mu, \phi, \mu', \phi')$ which corresponds to the redirection of radiation from (μ', ϕ') to (μ, ϕ), then the relative change in intensity can be written as

$$\begin{aligned} \mu \frac{\Delta I(z, \mu, \phi)}{\Delta z} = &-\beta_e I(z, \mu, \phi) + \beta_s F_0 e^{-\frac{\tau}{\mu}} \cdot \frac{P(\mu, \phi, \mu_0, \phi_0)}{4\pi} \\ &+ \beta_s \int_0^{2\pi} \int_{-1}^{1} I(z, \mu', \phi') \cdot \frac{P(\mu, \phi, \mu', \phi')}{4\pi} \mathrm{d}\mu' \mathrm{d}\phi' + \beta_a B[T(z)], \end{aligned} \tag{2.93}$$

in the case of radiative equilibrium, and with all of the terms previously discussed and defined. If the optical depth is here defined as

$$\tau = \int_z^{\infty} \beta_e \mathrm{d}z', \tag{2.94}$$

and the single-scattering albedo is

$$\tilde{\omega} = \frac{\beta_s}{\beta_e}, \tag{2.95}$$

and if the source function is

$$\begin{aligned} J(\tau, \mu, \phi) = &\frac{\tilde{\omega}}{4\pi} \int_0^{2\pi} \int_{-1}^{1} I(\tau, \mu', \phi') P(\mu, \phi; \mu', \phi') \mathrm{d}\mu' \mathrm{d}\phi' \\ &+ \frac{\tilde{\omega}}{4\pi} F_0 P(\mu, \phi, -\mu_0, \varphi_0) e^{-\frac{\tau}{\mu_0}} + (1 - \tilde{\omega}) B[T(\tau)], \end{aligned} \tag{2.96}$$

then Equation 2.93 can be rewritten as

$$\mu \frac{\mathrm{d}I(\tau, \mu, \phi)}{\mathrm{d}\tau} = I(\tau, \mu, \phi) - J(\tau, \mu, \phi). \tag{2.97}$$

It can often be assumed that the main parameters of this radiation transfer, i.e. the extinction coefficient, single-scattering albedo and phase function are independent of τ.
To closer define the phase function (which represents the angular distribution of scattered energy), we first relate the scattering angle Θ to the incoming and outgoing directions with

$$\cos\Theta = \mu\mu' + (1 - \mu^2)^{1/2}(1 - \mu'^2)^{1/2} \cos(\phi' - \phi), \tag{2.98}$$

in the case of spherical geometry. The phase function can be written using Legendre polynomials, as

$$P(\cos\Theta) = \sum_{l=0}^{N} \tilde{\omega}_l P_l(\cos\Theta), \tag{2.99}$$

where

$$\tilde{\omega} = \frac{2l+1}{2} \int_{-1}^{1} P(\cos\Theta) P_l(\cos\Theta) \mathrm{d}\cos\Theta, \tag{2.100}$$

with l ranging from 0 to N. When $l = 0$, $\tilde{\omega}_0 = 1$, which is the normalization of the phase function, and when $l = 1$

$$g = \frac{\tilde{\omega}_1}{3} = \frac{1}{2} \int_{-1}^{1} P(\cos\Theta) \cos\Theta \mathrm{d}\cos\Theta. \tag{2.101}$$

g is called the asymmetry factor, and is zero for symmetric scattering and Rayleigh scattering. For Lorenz-Mie scattering, it denotes the relative strength of the forward scattering.

Single-scattering case

If optical depths are smaller, i.e. of order $\tau < 0.1$, then most scattering can be represented just by single-scattering of a stellar beam. This condition is met usually for optically thin atmospheres with cirrus or aerosols. In this case, the source function can be simplified to

$$J(\tau, \mu, \phi) \simeq \frac{\tilde{\omega}}{4\pi} F_0 P(\mu, \phi, -\mu_0, \phi_0) e^{-\frac{\tau}{\mu}}, \tag{2.102}$$

and if we have a surface with no reflected upward intensity, and τ_* is the total optical depth, then the upward intensity at the top of the atmosphere will be

$$\begin{aligned} I(0, \mu, \phi) &= \int_0^{\tau_*} J(\tau', \mu, \phi) e^{-\frac{\tau'}{\mu}} \frac{\mathrm{d}\tau'}{\mu} \\ &= \frac{\mu_0 F_0}{\pi} \frac{\tilde{\omega}}{4(\mu + \mu_0)} P(\mu, \phi, -\mu_0, \phi_0) \left[1 - e^{-\tau_* \left(\frac{1}{\mu} + \frac{1}{\mu_0}\right)}\right]. \end{aligned} \tag{2.103}$$

With small total optical depths, the nondimensional bidirectional reflectance R can be defined as well, with

$$R(\mu, \phi, \mu_0, \phi_0) = \frac{\pi I(0, \mu, \phi)}{\mu_0 F_0} = \tau_* \frac{\tilde{\omega}}{4\mu\mu_0} P(\mu, \phi, -\mu_0, \phi_0). \tag{2.104}$$

This quantity has an application in retrieving aerosol optical depth in the Earth's atmosphere from satellites.

2.3.6 Line-by-line integration

In section 2.2 the mechanisms of formation of different spectral lines have been examined. From quantum mechanics models and laboratory measurements, the spectral lines of different absorbing species are known. Here we will explore one method of combining the effect of the individual lines to get the total absorption at each wavelength. The total optical depth is

$$\tau = \sum_{j=1}^{N} \tau_j = \int_u \sum_{j=1}^{N} k_{\nu,j}(u) \mathrm{d}u, \tag{2.105}$$

with j denoting the index of the absorption coefficient of the jth line. The absorption coefficient k_ν is

$$k_\nu(p, T) = \sum_{j=1}^{N} S_j(T) f_{\nu,j}(p, T), \tag{2.106}$$

where p is the pressure, T, the temperature, S_j the line strength and $f_{\nu,j}$ the line shape. To be able to resolve the individual lines, k_ν must be computed at wavelength intervals that are smaller than the half-width of the line. When dealing with infrared radiative transfer, it proves useful to use a small enough spectral interval, so that the Planck function variation within this interval can be neglected. The spectral transmittance can then be defined as

$$T_{\bar{\nu}}(u) = \int_{\Delta\nu} e^{-\tau} \frac{\mathrm{d}\nu}{\Delta\nu} = \int_{\Delta_\nu} \exp\left(- \int_u \sum_j k_{\nu,j}(u) \mathrm{d}u \right) \frac{\mathrm{d}\nu}{\Delta\nu}. \tag{2.107}$$

Because the absorption coefficient is a function of line strength and shape, which are functions of temperature and pressure, the line-by-line calculation of transmittance require a lot of computational power. Different methods are used to simplify these calculations and make them more economic.
To calculate the flux, the diffuse transmittance is needed:

$$T_\nu^f(\tau) = 2 \int_0^1 T_\nu \left(\tau/\mu\right) \mu \mathrm{d}\mu, \tag{2.108}$$

and usually it can be approximated as

$$T_{\bar{\nu}}^f \simeq T_{\bar{\nu}} \left(u/\bar{\mu}\right), \tag{2.109}$$

with $\bar{\mu}$ being the mean emergent angle, and the inverse of it being called the diffusivity factor.

Another approach to computing infrared radiative transfer is the correlated k-distribution method, which groups transmittances with regard to the absorption coefficient k_ν. It is beyond the scope of this work.

3
Methods and tools

In this chapter I explain how I interpreted an observed transmission spectrum through inverse modelling techniques. I will show the spectral retrieval of the Spectrum of WASP-39 an Ultra Hot Jupiter observed with the NIRSpec camera on board of James Webb Space Telescope (Rustamkulov et al. 2023) and a full interpretation of its atmosphere using a Bayesian Framework.

This chapter will briefly describe the telescope and instruments used to observe this spectrum (section 3.1). Then, the employed methods and frameworks will be explained in detail, namely the TauREx 3 Bayesian retrieval framework [27] (detailed in section 3.2), and the model selection methods with a focus on the nested sampling algorithm MultiNest [28] (in section 3.4), which were used to conduct atmospheric retrievals, as well as the TauREx-2D modelisation [17] (discussed in section 3.3) which was used for constructing and retrieving two-dimensional atmospheric models.

3.1 Telescope, instruments, and spectrum

3.1.1 JWST

The James Webb Space Telescope is a space observatory built by the National Aeronautics and Space Administration (NASA), the European Space Agency (ESA), and the Canadian Space Agency (CSA). It has a 6.5m gold-coated primary mirror and four instruments, these being the Near Infrared Camera (NIRCam), Near Infrared Spectrograph (NIRSpec), Near Infrared Imager and Slitless Spectrograph (NIRISS) and the Mid-Infrared Instrument (MIRI). The telescope is currently the most advanced space-based facility for infrared photometry and spectroscopy. It significantly improved observational capabilities for a number of astrophysical fields, one of these being exoplanetary atmospheres. The set of all the instruments present on JWST cover a wavelength range of 0.6μm to 28.5μm.

NIRSpec

The NIRSpec is one of the instruments of JWST, and the one used to obtain the spectrum used in this work. It covers a wavelength range from 0.6μm to 5.3μm. This instrument has a field of view of around 9arcmin^2, is capable of performing multiple-object spectroscopy (up to 100 objects at once) and can operate at spectral resolutions of 100, 1000 and 2700, using a low-resolution prism for the first and multiple medium- and high-resolution gratings for the others. Its observing modes are:

- Multi-object spectroscopy (MOS) with the micro-shutter assembly (MSA),
- Imaging spectroscopy with the integral field unit (IFU),
- High contrast single object spectroscopy with the fixed slits (FSs),
- High throughput bright object time-series (BOTS) spectroscopy with the NIRSpec wide aperture.

3.1.2 Spectrum

To obtain a spectrum from raw observational data, multiple reduction and calibration steps are required. These steps are usually packaged into different pipelines. Examples of these are FIREFLy [29], tshirt [30], Eureka! [31] or Tiberius [32].

The spectrum of WASP-39b modelled in this work (Figure 3.1) has been observed by the JWST NIRSpec instrument in BOTS prism. It is an observation of one transit, with a duration of 8.26h centered around the transit event. The raw data was reduced using different pipelines as a control, and they were all consistent. For the reduction of a saturated region of the spectrum, custom steps needed to be applied, and doing so enabled that region to be reduced as well. The details of the different reduction pipelines and procedures can be seen in Rustamkulov et al. 2023.

The aforementioned spectrum is public and was downloaded through the NASA Exoplanet Archive, selecting for the central wavelength, planet-star radius ratio, and the planet-star radius ratio error columns. Because the TauREx framework expects the squared planet-star radius ratio, the values were converted accordingly.

3.2 TauREx retrieval framework

The principal and central tool for this work is **TauREx** (Tau Retrieval for Exoplanets), which is an open source Bayesian framework for the retrieval of exoplanetary atmospheres. It is an extensive tool for creating forward models - i.e. creating spectra of atmospheres based on input parameters. A retrieval, on the other hand, would entail comparing a multitude of forward models with different parameter value combinations (within specified bounds), to then choose the best forward model with regard to an input (either real or synthetic) spectrum. There are various methods for finding and choosing the best model. The TauREx retrieval code, as other commonly used codes such as ArCis [33], Nemesis [34], Chimera [35], PyratBay [36] etc, uses a Bayesian approach for its inverse modeling procedure.

The details of the different input parameters and how they aggregate together in TauREx to form a model of

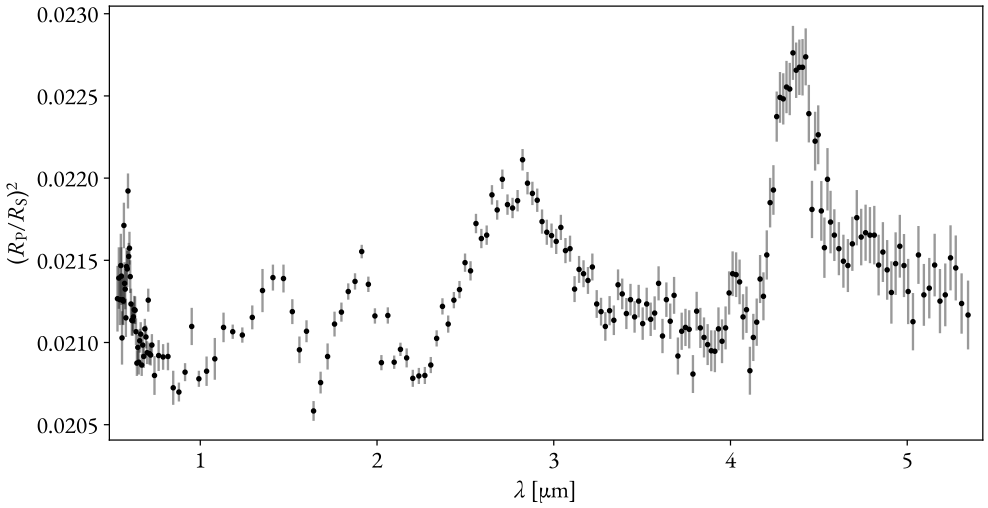

Figure 3.1: JWST NIRSpec prism spectrum of the atmosphere of WASP-39b (Rustamkulov et al. 2023)[7]. Publicly available through the NASA Exoplanet Archive.

an atmospheric spectrum will be explained in this section. It should be noted that the atmospheres modelled here consider the parameters to vary only along a single direction, that is with the altitude in the atmosphere, and have no variations with regard to day-night differences. These are accounted for in TauREx 2D (section 3.3).

3.2.1 Components of a TauREx forward model

While TauREx can be used as a **python** library, it is usually controlled using so-called parfiles (parameter files). These files contain the values for all the parameters that go towards building the forward model, while non-specified parameters usually take some default value (if they are needed for the creation of a model). Within these files one would also specify an observation file (if present), other required files, whether the forward model will be fitted to this observation or not, and which fitting method will be applied. If fitting is performed, then priors and boundaries for the fitted parameters need to be specified. All the components of a parfile will be elaborated upon in the rest of this subsection.

Global section

In the global section one specifies paths to all the needed cross sections, as well as the methods for cross section interpolation (for temperature). Whether or not multiple cores should be used in retrievals will also be specified in this section. Generally, this section contains information about setting that affect the entire program.

Chemistry

The chemistry section contains all of the information on the chemical composition of the exoplanetary atmosphere whose forward model will be built. It also contains information about what type of chemistry will be used. TauREx has some built in chemical models, as well as several officially supported plugins, but also accepts custom chemistries.

In this work I used two possible chemical configurations: "free" chemistry and equilibrium chemistry using **FastChem** [37]. The "free" chemistry describes a set of independent molecular mixing ratios constant throughout all of the atmospheric layers, while equilibrium chemistry calculates the most probable abundances based on the physical parameters of the atmosphere, so that the atmosphere is in chemical equilibrium. In order to reproduce the **FastChem** results for a gas in chemical equilibrium I used the taurex-fastchem plugin. Chemical equilibrium means that the concentrations of reactants and products of the chemical reactions that might occur in the atmosphere remain constant with time.

In the case of free chemistry, the absorbing chemical species are specified, their volume mixing ratios, and whether the abundances are constant throughout the atmosphere or have different values at two levels (i.e. single-level or two-level abundances). These abundances can be fitted when retrieving an atmosphere.

For equilibrium chemistry, usually a ratio of two elements (e.g. carbon to oxygen, C/O) can be fitted, while the abundances of the absorbing species are retrieved based on chemical equilibrium and this ratio, as well as the metallicity.

Temperature and pressure

In the temperature and pressure sections, the type of temperature-pressure profile needs to be specified. The simplest temperature profile is the isothermal one (which has the same temperature in the entire atmosphere), however, a number of other profiles are built into TauREx, such as the Guillot profile [38], n-point profiles, or layer-by-layer profiles. The temperature-pressure profile can also be specified from a file. For an isothermal profile, only one temperature value is specified, while for the npoint profile n values will be specified. The other models have their own different parameters.

In this work usually an isothermal or 4-point profile was used, while the pressure was set to a 100-layer model with provided maximum and minimum pressures. The pressure profile is most often a simple one, calculated at every layer boundary as an equally logarithmically spaced value, and using these values the value of the pressure at each boundary is calculated by

$$P_l = p_l \sqrt{\frac{p_{l+1}}{p_l}}, \tag{3.1}$$

p being the pressures at the layer boundaries and P_l the pressure in the layer.

Planet

The planet section contains the parameters of the exoplanet, namely its mass and radius (in Jupiter masses and radii). Values of the orbital parameters of the planet can also be specified, these being:

- star-planet distance (in AU),

- impact parameter,
- orbital period (in days),
- albedo,
- transit time (in seconds).

Star

The first parameter of the star section is that of star type. TauREx supports either black body or PHOENIX [39] star types, as well as custom ones (like for all the other sections). Depending on the star type, other parameters are available. If the star is a black body, then the following parameters can be set:

- temperature (in kelvin),
- radius (in solar radii),
- mass (in solar masses),
- distance from Earth (in pc),
- metallicity (in solar units),
- magnitude in the K-band.

If the stellar type is PHOENIX, the path to the PHOENIX directory is supplied as well as all the parameters previously listed. All of these values are optional and have their default values. In this work, the star was considered a black body in all cases.

Model

This section supplies information on the type of the forward model, and the physical contributions of said model. The model type can be transmission, emission, direct-image, or a custom one, as with all the other sections. The contributions to the model can be:

- molecular absorption,
- CIA (with specified CIA pairs),
- Rayleigh scattering,
- clouds (with specified and fittable pressure in Pa),
- Mie scattering (with appropriate parameters).

One can select just a single of these contributions to the model, and not all of them are necessary. For example, a transmission model with just molecular absorption can be created.

Observation

The observation file supplied to TauREx in this section can either be an observed spectrum (3 or 4 columns - wavelength, depth, error, widths), a lightcurve pickle file, an Iraclis pickle spectrum or a taurex spectrum. The taurex spectrum enables self-retrievals, or retrievals from a HDF5 TauREx output file.

Optimizer

In this section one chooses the optimizer to be used and sets its specific parameters. The TauREx program supports several different samplers, those being:

- `nestle`,
- MultiNest,
- `PolyChord` [40],
- `dyPolyChord` [41],

along with supporting custom samplers. The sampler used throughout this work is the nested sampler MultiNest. The nested sampling technique will be explored in section 3.4, while MultiNest and its parameters will be detailed upon in subsection 3.4.2.

Fitting

In the fitting section one will choose among the available parameters those that they wish to fit. Here, the priors and prior ranges are to be set as well. The prior distributions supported are uniform, log-uniform, Gaussian and log-Gaussian. The parameter bounds can be set either as linear or logarithmic values, for the first two distribution, while the latter two require a mean and standar deviation value.

3.2.2 Forward model creation

There are several steps to building a forward model based on all the components listed in the previous subsection. Firstly, the atmosphere is divided into layers based on altitude, where the altitude profile at each layer is computed as follows:

$$\begin{aligned} z_l &= z_{l-1} + \Delta z_l, \\ \Delta z_l &= -H_{l-1} \log\left(\frac{P_l}{P_{l-1}}\right), \\ H_l &= \frac{k_B T_l}{\mu_l g_l}, \\ z_0 &= 0, \end{aligned} \tag{3.2}$$

where z_l is the altitude of the layer, l is the layer index, the layer at $l = 0$ being the bottom of the atmosphere (at the planetary radius), k_B Boltzmann's constant, H_l is the scale height, T_l the temperature at layer l, provided by the temperature profile, P_l the pressure at layer l, provided by a pressure profile, μ_l is the mean molecular weight and g_l the gravitational acceleration.

Transmission models

The atmosphere for transmission (transit) spectra in TauREx is one-dimensional and the altitude is parametrized by layers. The total depth at a certain wavelength is given by

$$\Delta_\lambda = \frac{R_\mathrm{p}^2 + a_\lambda}{R_\mathrm{s}^2}, \tag{3.3}$$

R_p being the planetary radius, R_s the stellar one and a_λ a wavelength-dependent depth, defined by

$$a_\lambda = \int_0^{z_\mathrm{max}} (R_\mathrm{p} + z \left(1 - e^{\tau_\lambda(z)}\right) \mathrm{d}z, \tag{3.4}$$

with z_max denoting the top of the atmosphere, and all other quantities previously defined. The total optical depth at wavelength λ is defined as the sum of the optical depths of each absorber and contribution, while the individual absorber optical depths are given by

$$\tau_{\lambda,i} = \int_z^{z_\mathrm{max}} \sigma_{\lambda,i}(z')\chi_i(z')\rho(z')\mathrm{d}z', \tag{3.5}$$

in the case of molecular absorption, where $\sigma_{\lambda,i}$ is the cross section of an absorbing species, χ_i the column density of that species and ρ the number density.

In the case of collisionally induced absorption, on the other hand, which involves pairs of molecules, $\tau_{\lambda,i}$ is given by

$$\tau_{\lambda,i} = \int_z^{z_\mathrm{max}} \sigma_{\lambda,i}(z')\chi_i(z')\chi_i'(z')\rho(z')^2\mathrm{d}z', \tag{3.6}$$

now having contributions from the column densities of both species.

The contribution to the optical depth from clouds is simply

$$\tau_\mathrm{clouds}(\lambda, z) = \begin{cases} \sigma & \text{if } P_t \geq P(z) \geq P_b \\ 0 & \text{if } P(z) < P_b \\ 0 & \text{if } P(z) > P_t \end{cases} \tag{3.7}$$

with σ being a user-defined opacity, P_t pressure at the top of the cloud deck and P_b the pressure at its bottom.

Emission models

In the case of an emission (eclipse) spectrum, the atmosphere is considered to be plane-parallel. The emission from each layer is integrated to get the emission at the top of the atmosphere, which, seen at angle θ, is given by:

$$I_\lambda(\tau = 0, \mu) = B_\lambda(T_s)e^{-\frac{\tau_s}{\mu}} + \int_0^1 \int_0^{\tau_s} B_\lambda(T_\tau)e^{-\frac{\tau}{\mu}}\mathrm{d}\tau\mathrm{d}\mu, \tag{3.8}$$

where T_s is the temperature at the maximum pressure, and B_λ is the Planck function, τ_s the total optical depth, and all other quantities have been previously defined. The integration with regard to the viewing angle is done

using an N-point Gauss-Legendre quadrature scheme, and the final emission spectrum is given by

$$\frac{F_p}{F_s} = \frac{I_\lambda(\tau = 0)}{I_s} \times \left(\frac{R_p}{R_s}\right)^2. \tag{3.9}$$

Cross sections

The cross sections are obtained from ExoMol [42], a database of high temperature molecular line lists for modelling exoplanet atmospheres. The approach used for creating these line lists is a mixture of first principles and empirically tuned quantum mechanical methods, while the spectra are generated from these lists using the ExoCross [43] algorithm.

Cross sections are usually provided in temperature-pressure-wavelength grids, i.e. they are discreet. To have cross sections at every temperature or pressure value, interpolation is performed. Two methods for interpolation exist in TauREx; a linear, simple one, and an exponential one. Linear interpolation is performed as

$$\sigma_i(T) = \sigma_i(T_1) + m(T - T_1), \tag{3.10}$$

with

$$m = \frac{\sigma_i(T_2) - \sigma_i(T_1)}{T_2 - T_1}, \tag{3.11}$$

and analogously for pressure interpolation. T is the temperature at which one wishes to have a cross section value, while T_1 and T_2 are adjacent values with available cross section values. The exponential method of Hill et al. 2013 [44], on the other hand, comprises of:

$$\begin{aligned} \sigma_i(T) &= a_i e^{-b_i/T}, \\ b_i &= \left(\frac{1}{T_2} - \frac{1}{T_1}\right) \ln \frac{\sigma_i(T_1)}{\sigma_i(T_2)}, \\ a_i &= \sigma_i(T_1) e^{b_i/T_1}. \end{aligned} \tag{3.12}$$

It is more precise, but takes about three times more time to compute. The default method in TauREx is the linear one. In the case where the required temperature/pressure is above or below the known temperature/pressure range for the given cross section, it is fixed to either the maximum or minimum known temperature/pressure, respectively.

3.3 TauREx 2D

TauREx-2D [17] is a plugin for TauREx that enables the creation of two-dimensional atmospheric transmission models, in contrast to the one-dimensional ones built within TauREx. While it implements this new depth to the models, it is still controlled in the same way as base TauREx, through parameter files.

It adds new, 2D model types to the previously described temperature, chemistry, and model sections, by differentiating between dayside, nightside and "deep" (i.e. above a certain pressure value) values for the temperature and abundances of chemical species. Models built in this way should provide a more accurate representation of

the spectra of planets that are close enough to their host stars so that the day-night differences are pronounced enough to be detected by current instruments.

3.3.1 Forward model creation

The models built by TauREx-2D assume symmetry with regard to the star-observer axis. The pressure, and therefore layers of the atmosphere, is parametrized in the same way as in TauREx, while the temperature is then two-dimensional, being dependent on the layer (i.e. pressure) and angular coordinate. It is defined as such

$$\begin{cases} P > P_{\text{iso}}, & T = T_{\text{deep}}, \\ P < P_{\text{iso}}, & \begin{cases} 2\alpha^* \geq \beta, & T = T_{\text{day}}, \\ 2\alpha^* \leq -\beta, & T = T_{\text{night}}, \\ -\beta < 2\alpha^* < \beta, & T = T_{\text{night}} + (T_{\text{day}} - T_{\text{night}}) \frac{\alpha^* + \beta/2}{\beta}, \end{cases} \end{cases} \tag{3.13}$$

where α^* is the angular coordinate and β is an angle parameter that defines the scale of the transition zone between the day and night sides of the atmosphere, and P_{iso} is the pressure beneath which the atmosphere is considered isothermal. These assumptions are made based on Global Climate Models (GCM), in particular the, LMDZ-inspired (*Laboratoire de Météorologie Dynamique Zoom*) GCM models.

Afterwards, the pressure, temperature and abundances are interpolated in a grid that is based on altitude, thus having now a new coordinate system that is (α^*, z). Then, the incoming radiation is parametrized by rays, a single ray for each atmospheric layer, which has length $\Delta l_{r,i}$ where r is the ray index and i is the index of the layer the ray is crossing. Then, the optical depth for each ray will be

$$\tau_\lambda^r = \sum_i \frac{P_{r,i}}{k_{\text{B}} T_{r,i}} \left(\sum_{\text{m}=1}^{N_{\text{gas}}} \chi_{\text{m},r,i} \sigma_{\text{m},\lambda} + \sum_{j=1}^{N_{\text{con}}} k_{\text{Mie},j} \right) \Delta l_{r,i}, \tag{3.14}$$

where $P_{r,i}$ is the pressure and $T_{r,i}$ the temperature of the segment i of ray r, $\chi_{\text{m},r,i}$ is the mixing ratio of molecule m, $\sigma_{\text{m},\lambda}$ the collective cross section of molecular and continuum absorptions, as well as Rayleigh scattering, and $k_{\text{Mie},j}$ is the Mie scattering cross section of the j-th aerosol. CIA is also included, for $H_2 - H_2$ and $H_2 - He$ pairs. There are two chemistry modes within this plugin. One is free chemistry, where the mixing ratios of species are constant in each respective sector (day, night, or deep). The other chemistry mode is thermal dissociation of molecular species, based on Parmentier et al. 2018 [15]. In this case, the deep abundances are considered a parameter, while the day/night abundances are computed based on based on the local pressure and temperature. All the new parameters specified here (e.g. β, P_{iso}, the different abundances) can be expressed as free parameters and can be retrieved by TauREx.

3.4 Parameter estimation and model selection

Bayesian inference methods are commonly used to estimate the parameters of a model, or to choose a model. The purpose of any of these methods is to determine the parameters or model with the highest probability. The most common Bayesian inference method is Markov Chain Monte Carlo (MCMC), but this method is very computationally intensive. To understand the meaning of model inference and the different methods used to assess it, one should start from Bayes' theorem

$$p(\mathbf{\Theta}|\mathbf{D},\mathcal{M}) = \frac{p(\mathbf{D}|\mathbf{\Theta},\mathcal{M})p(\mathbf{\Theta}|\mathcal{M})}{p(\mathbf{D}|\mathcal{M})}. \tag{3.15}$$

Here, $\mathbf{\Theta}$ is a set of model parameters, $\mathbf{D}$ is the observed data and $\mathcal{M}$ is the model (hypothesis). The different probabilities can also be written as

$$\begin{aligned} p(\mathbf{\Theta}|\mathbf{D},\mathcal{M}) &\equiv \mathcal{P}(\mathbf{\Theta}),\\ p(\mathbf{D}|\mathbf{\Theta},\mathcal{M}) &\equiv \mathcal{L}(\mathbf{\Theta}),\\ p(\mathbf{\Theta}|\mathcal{M}) &\equiv \pi(\mathbf{\Theta}),\\ p(\mathbf{D}|\mathcal{M}) &\equiv \mathcal{Z}, \end{aligned} \tag{3.16}$$

$\mathcal{P}(\mathbf{\Theta})$ being the posterior probability distribution of the parameters (i.e. the probability of having the parameters $\mathbf{\Theta}$ given data $\mathbf{D}$ and model $\mathcal{M}$), $\mathcal{L}(\mathbf{\Theta})$ the likelihood (i.e. the probability of having the data given the parameters and model), $\pi(\mathbf{\Theta})$ the prior (i.e. the prior probability of the parameters given the model), and $\mathcal{Z}$ the evidence (i.e. the probability of having the data given the model). For parameter estimations, the evidence is usually ignored, as it is independent of $\mathbf{\Theta}$. For model estimation, however, it is crucial. It is the factor that normalizes the posterior distribution over the parameter space:

$$\mathcal{Z} = \int \mathcal{L}(\mathbf{\Theta})\pi(\mathbf{\Theta})\mathrm{d}^D\mathbf{\Theta}, \tag{3.17}$$

where D is the number of dimensions of the parameter space. This also ensures that a simpler model (i.e. with a more compact parameter space) will always have a higher evidence, unless the more complex model is really better at explaining the data at hand. To evaluate the evidence using Equation 3.17 is difficult, as this is a multidimensional integral. It is done numerically, and using the technique of thermodynamic integration, an order of 10^6 MCMC samples are needed to achieve a satisfactory accuracy of the determined evidence, for each chain. The nested sampling technique aims to reduce the cost of and speed up this calculation.

3.4.1 Nested sampling

Nested sampling is a Monte Carlo method for the calculation of the Bayesian evidence. It also, coincidentally, infers the posteriors. It is based on the existence of a relation between the likelihood and the prior volume, which enables the integral from Equation 3.17 to be transformed into a one-dimensional one. The prior volume

is defined by

$$\begin{aligned} \mathrm{d}X &= \pi(\boldsymbol{\Theta})\mathrm{d}^D\boldsymbol{\Theta}, \\ X(\lambda) &= \int_{\mathcal{L}(\boldsymbol{\Theta})>\lambda} \pi(\boldsymbol{\Theta})\mathrm{d}^D\boldsymbol{\Theta}, \end{aligned} \tag{3.18}$$

with the integration over the region of the parameter space within an iso-likelihood contour defined by $\mathcal{L}(\boldsymbol{\Theta}) = \lambda$. This transforms the integral from Equation 3.17 into

$$\mathcal{Z} = \int_0^1 \mathcal{L}(X)\mathrm{d}X, \tag{3.19}$$

$\mathcal{L}(X)$ being the inverse of $X(\lambda)$, and is a monotonically decreasing function of X. Therefore, by determining the likelihood $\mathcal{L}_i$ at a certain number of points X_i, numerically the evidence can be obtained using

$$\mathcal{Z} = \sum_{i=1}^{M} \mathcal{L}_i w_i, \tag{3.20}$$

where w_i are weights, which are given by

$$w_i = \frac{1}{2}(X_{i-1} - X_{i+1}). \tag{3.21}$$

First, a sample of so-called live points is drawn from the entire prior $\pi(\boldsymbol{\Theta})$. Then, the point with the lowest likelihood ($\mathcal{L}_0$) is excluded, becomes inactive, and is replaced by another point from the prior, but now with a constraint that its likelihood is larger than $\mathcal{L}_0$. This then happens at every subsequent step, replacing a point and reducing the prior volume from which the points are drawn. Considering the fact that the prior volume gets smaller at every step, the next prior is always "nested" within the previous one, hence the name nested sampling. These steps are repeated until a specified precision in the evidence is reached. At step i, the largest contribution to the evidence from the remaining set is

$$\Delta(Z)_i = \mathcal{L}_{\max} X_i, \tag{3.22}$$

with $\mathcal{L}_{\max}$ being the largest likelihood among the live points at step i.
After the evidence is determined, one can infer information on the posterior, using the weight

$$p_j = \frac{\mathcal{L}_j w_j}{\mathcal{Z}}, \tag{3.23}$$

where j runs through both the active and inactive points from the nested sampling algorithm.

The most difficult step of this procedure is implementing the constraint of $\mathcal{L} > \mathcal{L}_i$ at every iteration. An approach to this problem is that of ellipsoidal nested sampling (Mukherjee et al. 2006, [45]). The approach consists of simplifying the iso-likelihood contour ($\mathcal{L} = \mathcal{L}_i$), approximating it as a D-dimensional ellipsoid. This ellipsoid is determined from the covariance matrix of the current active points, and is then enlarged by some arbitrary factor. The new active points are then drawn from this ellipsoid, until a point such that its likelihood is larger than the one of the lowest likelihood (removed) point. This method is highly efficient if the posterior distribution is unimodal, but is not capable of separating different modes in multimodal posterior distributions.

3.4.2 MultiNest

The MultiNest algorithm aims to eliminate the limitations of the ellipsoidal nested sampling method. It starts from a unit hypercube of dimension D as the prior volume, unit meaning all parameters take values between 0 and 1. The points $\mathbf{u}$ drawn from these normalized priors need to be converted into the physical parameter space $\mathbf{\Theta}$, and this is governed by the relation

$$\int \pi(\theta_1, \theta_2, \ldots, \theta_D) \mathrm{d}\theta_1 \mathrm{d}\theta_2 \ldots \mathrm{d}\theta_D = \int \mathrm{d}u_1 \mathrm{d}u_2 \ldots \mathrm{d}u_D. \tag{3.24}$$

Usually, this transformation is simple (when the prior is separable), but is also solvable in other cases (either numerically or analytically). If the prior is uniform (which is a very common case), then the unit hypercube and physical parameter space are the same.

The next step is to divide the initial set of points into a number of clusters, and to create new ellipsoidal bounds for each of these clusters. If a set of active points in the initial unit hypercube is $S = \{\mathbf{u}_1, \mathbf{u}_2, \ldots, \mathbf{u_n}\}$ and it has a K-partition $\{S_k\}_{k=1}^{K}$, then, for a cluster containing n_k points, an approximation for its minimum volume bounding ellipsoid is:

$$E_k = \{\mathbf{u} \in \mathbb{R}^D | \mathbf{u}^T (f_k \mathbf{C}_k)^{-1} \mathbf{u} \geq 1\}, \tag{3.25}$$

with the empirical covariance matrix given by:

$$\mathbf{C}_k = \frac{1}{n_k} \sum_{j=1}^{n_k} (\mathbf{u}_j - \boldsymbol{\mu}_j)(\mathbf{u}_j - \boldsymbol{\mu}_j)^T, \tag{3.26}$$

To get the optimal decomposition of the original prior space into K ellipsoids, one must minimize

$$F(S) \equiv \frac{1}{V(S)} \sum_{k=1}^{K} V(E_k), \tag{3.27}$$

where $V(S)$ is the volume of the space from which the set S is uniformly sampled, and $V(E_k)$ is the volume of a bounding ellipsoid. This is performed using an expectation-minimization algorithm. Algorithms like this can be computationally expensive at higher dimensions, but MultiNest does not need to perform the full algorithm at every step. Instead, after the initial partitioning and construction of bounding ellipsoids, they can be evolved by scaling instead of new ones being created every time. They are scaled so that their volumes are $\max[V(E_k), X_{i+1}\frac{n_k}{N}]$, where X_{i+1} is the remaining prior volume in the next nested sampling iteration. Because it is expected for the algorithm to move towards higher likelihood regions with each step, the previous partition into ellipsoids becomes less optimal. In the case of $F(S) > h$, where usually $h = 1.1$, a new partitioning is performed.

If the ellipsoidal bounds created overlap in some regions, one must make sure that points that lie within more than one ellipsoid are sampled with the same probability as a point that lies within a single ellipsoid, because the end goal is to sample a points from the union of all the ellipsoids. Therefore, the probability of each sampled point being drawn is divided by the number of ellipsoids that the point lies in to ensure consistent sampling.

Considering some multimodal problems require a very large number of live points initially, this would cause convergence to be very slow. MultiNest enables the number of live points to decrease as the algorithm moves

towards higher likelihood regions. The number of live points is decreased as

$$N_i = N_{i-1} - N_{\min} \frac{\Delta Z_{i-1} - \Delta Z_i}{\Delta Z_i - \text{tol}}, \tag{3.28}$$

with

$$\Delta Z_i = \mathcal{L}_{\max} X_i \tag{3.29}$$

being the largest contribution to the evidence by the remaining portion of the posterior at iteration i, $N_{\min}$ is the minimum number of active points allowed and tol is the tolerance of the final evidence.

Finding different modes

If modes in the posterior are well-defined and isolated, MultiNest is capable of separating them, i.e. determining which samples belong to which mode. This also enables the evaluation of so-called local evidences for each mode. To do this, once the a high enough likelihood level is reached, if a mode has a high footprint in the total likelihood, in the next steps the points belonging to this mode will be selected among the total active points. The fact that the sample is already partitioned into clusters helps in this case.

The process is as follows: initially all the active points are grouped together. Once the initial set is divided into K subsets S_k, they are bounded by their ellipsoids E_k. At every step, one of the subsets and its corresponding ellipsoid is picked randomly, and all the other sets and ellipsoids are checked for overlapping with this chosen one. If this is the case, they are considered part of a new, bigger chosen ellipsoid (and subset). This is done until no more overlapping ellipsoids exist. If, after this, more ellipsoids exist outside of this group, the remaining active points are grouped together, and analyzed in a similar way as the initial group was, possibly splitting further. The whole process is continued until no more splitting can be done, and the nested sampling process continues. At every subsequent nested sampling step this process is repeated and new groups can be created, while old ones can become inactive. If, within a group, there are two ellipsoids that do not intersect, they will not be checked for intersection in any of the next steps.

The evidence of each identified separate mode can be calculated as

$$Z_l = \sum_{j=1}^{n_l} \mathcal{L}_j w_j, \tag{3.30}$$

where

$$w_j = \frac{X_M}{N} \tag{3.31}$$

for each active point in the mode M_l, and

$$w_j = \frac{1}{2}(X_{l-1} - X_{l+1}) \tag{3.32}$$

for each inactive point, where i is the index of the nested sampling iteration at which the inactive point was discarded. Posterior inferences can be obtained in the same way as when there was no mode separation (Equation 3.23). The only situation in which the evidence estimation might be underestimated is when the different

modes are close to each other, but this is solved using also the points in the inactive groups, at the end of the nested sampling process.

MultiNest in TauREx

MultiNest is the main sampler used for model selection within TauREx in this work. It is supported by TauREx natively. This sampling algorithm is useful for retrieving exoplanet atmospheres because it can occur that two or more possible solutions exist for some parameter values (e.g. Zingales et al. 2022, [19]), and MultiNest is well suited in separating them, instead of considering them as a single solution or, as it may happen with the MCMC algorithm, having the parameter values representing only a local solution.
The parameters of MultiNest to be used as a sampler within TauREx can be set inside a parfile. The parameters that the user sets are the following:

- the number of live points,
- whether to search for multiple modes,
- whether to use importance sampling,
- whether to resume a previously started sampling process.

MultiNest is also well suited to be parallelized, so therefore all TauREx retrievals (except a few initial, simpler ones) were ran on 10 to 40 cores on the **kraken** cluster at the Department of Physics and Astronomy "Galileo Galilei" in Padova, Italy.

3.5 Assessment of a model's statistical significance

When comparing models with different parameter sets and prior values, it is useful to have a measure of the statistical significance of each of them, and, even more importantly, a way to compare their relative goodness directly. Because MultiNest infers the Bayesian evidence and tries to maximize it for a given set of parameters and priors, this is the main resource used to compare different models. Recalling the definition of the Bayesian evidence from Equation 3.17 and Equation 3.16, it can be seen that it is the average of the likelihood under the prior, for a specific model. From the evidence and through the Bayes theorem one can obtain the model posterior probability given the data:

$$p(\mathcal{M}|\mathbf{D}) \propto p(\mathcal{M})\mathcal{Z}, \tag{3.33}$$

$p(\mathcal{M})$ being the a priori probability of a model. When comparing two models, one is interested in the ratio of these posterior probabilities:

$$\frac{p(\mathcal{M}_1|\mathbf{D})}{p(\mathcal{M}_2|\mathbf{D})} = B_{12}\frac{p(\mathcal{M}_1)}{p(\mathcal{M}_2)}, \tag{3.34}$$

where

$$B_{12} \equiv \frac{\mathcal{Z}_1}{\mathcal{Z}_2} \tag{3.35}$$

is the **Bayes factor**, the ratio of the models' evidences. If $B_{12} > 1$, model $\mathcal{M}_1$ is preferred, and vice-versa. The difference in goodness of these two models can be considered statistically significant if $\log B_{12} > 3$, which is

coincidentally equivalent to a difference of 3σ between the models [46]. A Bayesian model comparison will on its own favour simpler models that adequately explain the data at hand, and will give the answer to whether a more complex model is needed or not. If it happens, regardless, that Bayes factor for two models of varying complexity is statistically insignificant, Occam's razor will be applied and the simpler model will be chosen.

4

Models and results

In this chapter I will discuss the atmospheric models retrieved using the methods described in chapter 3, starting from the simple initial guesses – one-dimensional, constant chemistry isothermal models – through more complex and realistic one-dimensional models, equilibrium chemistry models as well as two-dimensional, isothermal ones.

The statistical significance of these models will be compared, using the Bayes factor, and conclusions will be drawn from the most probable models out of the ones created. Within this chapter I will describe the details of each model, their limits and their advantages in the characterization of the atmosphere of WASP-39b.

4.1 Model parameters

Several parameters of the exoplanet have been determined from the transmission spectrum of its atmosphere. Depending on the model assumption, different parameter sets were used. These parameters have been fitted and their best-fit values have been determined using the methods described in chapter 3, and their solutions will be presented in section 4.3, after a discussion of the models from which they have been obtained.

Some parameters of the exoplanet and its host star cannot be derived from the transmission spectrum, and these parameters were assigned fixed values. These are the planetary mass M_P, stellar effective temperature T_{eff} and stellar radius R_S, which were all taken from Mancini et al. 2018 [47].

Along with these, the ratio of the main fill gases, which are H_2 and He, was fixed to the standard value (85% H_2 and 15% *He*) in the main models. The reasoning behind this was Occam's razor, as the models which had this parameter fixed had an equivalent statistical significance as the ones that had it fitted, so the simpler option was chosen. The star was modelled as a black body throughout all models. All of the fixed parameter values are given in Table 4.1.

The models included molecular and atomic absorption, Rayleigh scattering, simple clouds, and collision-induced

Table 4.1: Fixed model parameters and their values. The He/H_2 ratio is a standard value, and the rest of the values are from Mancini et al. 2018 [47]. M_J is the mass of Jupiter and $R_\odot$ is the radius of the Sun.

Parameter	Value
He/H_2 ratio	0.17647
T_{eff}	5485 K
R_S	$0.939\ R_\odot$
M_P	$0.281\ M_J$

absorption by H_2-H_2 and H_2-He pairs, unless otherwise stated.

4.2 Models

The initial models created were the simplest ones, and then the complexity of the models was gradually increased. The models are for the most part one-dimensional, meaning that if the atmospheric parameters vary, they do so only along one direction, that is the altitude in the atmosphere (and consequently, they do not vary with latitude and longitude).

The two-dimensional models created, on the other hand, take into account a longitudinal (day to night) variation, while also keeping the variation of the parameters along the altitude axis.

4.2.1 One-dimensional models

1D models with free chemistry

The first set of models, accounting for the majority of all the models created, are one-dimensional models with a single-level free chemistry. A free chemistry in this context means that the mixing ratios of chemical species assume individual, independent (i.e. "free") profiles throughout the atmosphere. These profiles are in this case constant, i.e. the mixing ratio of every chemical species has one constant value.

The initial 1D models were created with few chemical species, namely H_2O, CO_2, and CO, as these were the chemical species previously detected in this exoplanet with a very large certainty. These models had an isothermal temperature-pressure (T-P) profile, and were quickly dismissed as too simple, in favour of slightly more complex ones. For a summary of all the models, one should refer to Table 4.2.

The simplest model that is still worth considering is one with a Guillot 2010 temperature profile, absorption, Rayleigh scattering, H_2 and He as fill gases, and with CO, CO_2, H_2O and TiO as absorbing molecules. TiO was added in this model to try to explain the stronger absorption in the lowest wavelength regions of the spectrum. This is Model 1 in Table 4.2. The fitted spectrum and T-P profile of this model can be seen in Figure 4.1.

Afterwards, an even more complex T-P profile was tested, namely a 4-point one, but without changing the other fitting parameters. This is Model 2 and is shown in Figure 4.2.

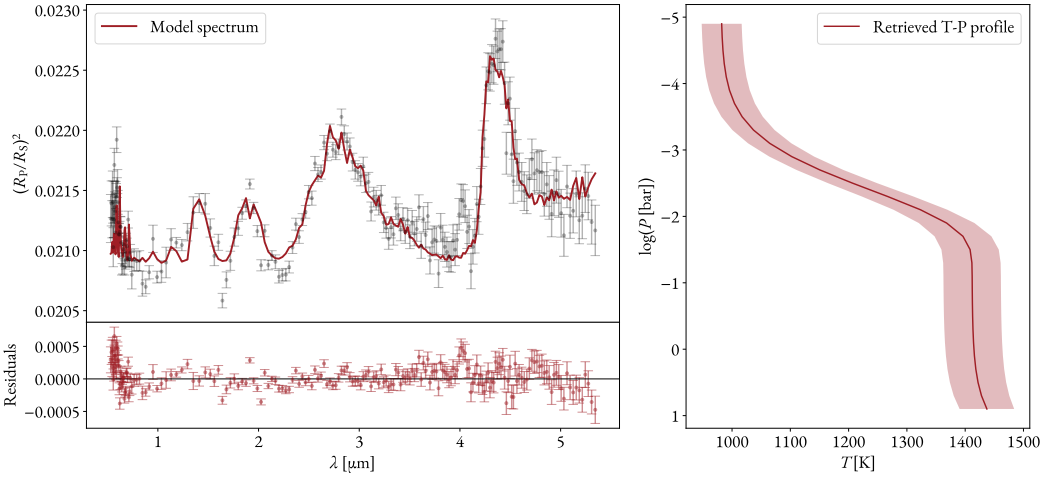

Figure 4.1: Fitted spectrum (left) and temperature-pressure profile (right) of Model 1. This model fits the He/H_2 ratio and does not include CIA. It has a Guillot T-P profile

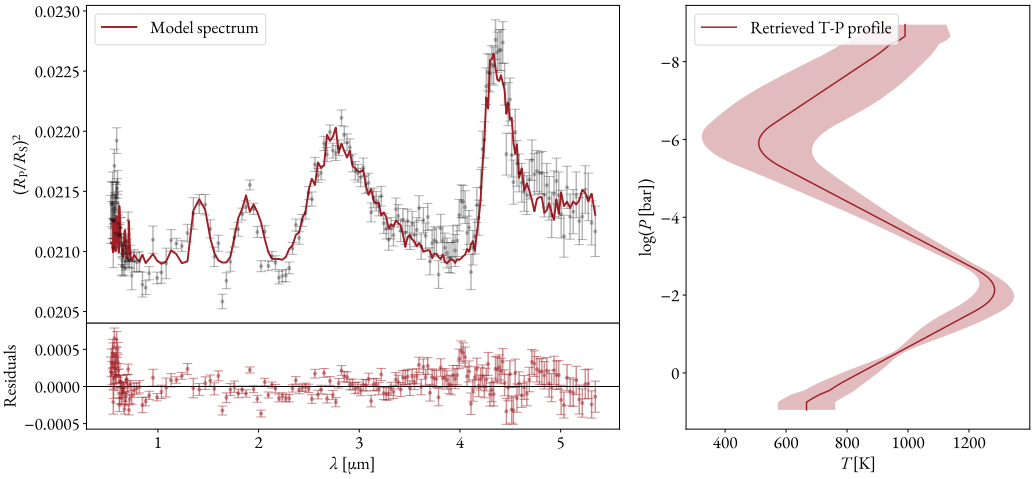

Figure 4.2: Fitted spectrum (left) and temperature-pressure profile (right) of Model 2. This model fits the He/H_2 ratio and does not include CIA. It has a 4-point T-P profile.

Then, in Model 3 (Figure 4.3), VO was added, as well as collision-induced absorption, keeping the T-P profile as a 4-point one, but this resulted in a less certain determination of the profile itself.

In Figure 4.4, the spectrum of Model 4 can be seen. This model, compared to Model 3 has the addition of H_2S as an absorbing species. A very similar model to Model 4 is Model 5, which can be seen in Figure 4.5, with the only difference being that Model 5 does not fit the He/H_2 ratio. This was used to asses whether there is a need to

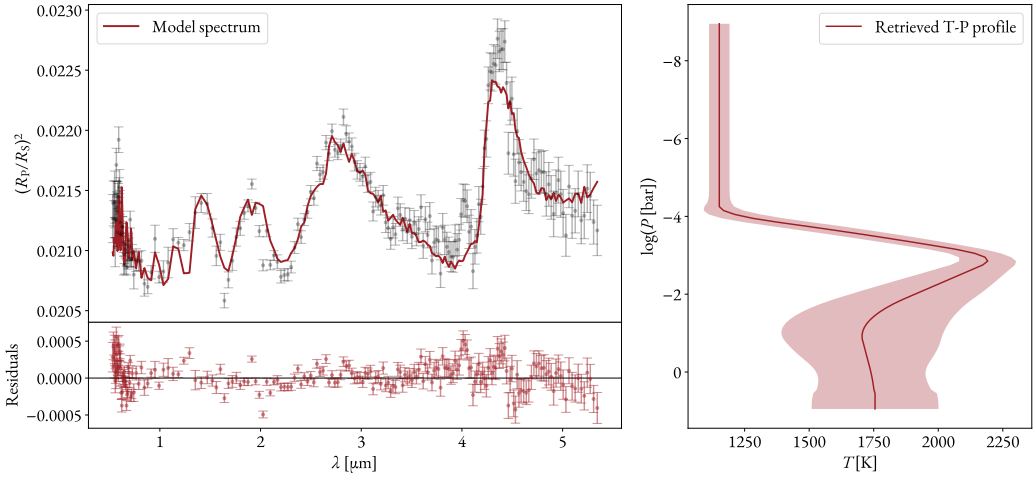

Figure 4.3: Fitted spectrum (left) and temperature-pressure profile (right) of Model 3. This model fits the He/H_2 ratio and includes CIA, with a 4-point T-P profile.

fit this ratio or not - the conclusion was that it is not necessary, judging by the insignificant Bayes factor between these two models (see Table 4.2).

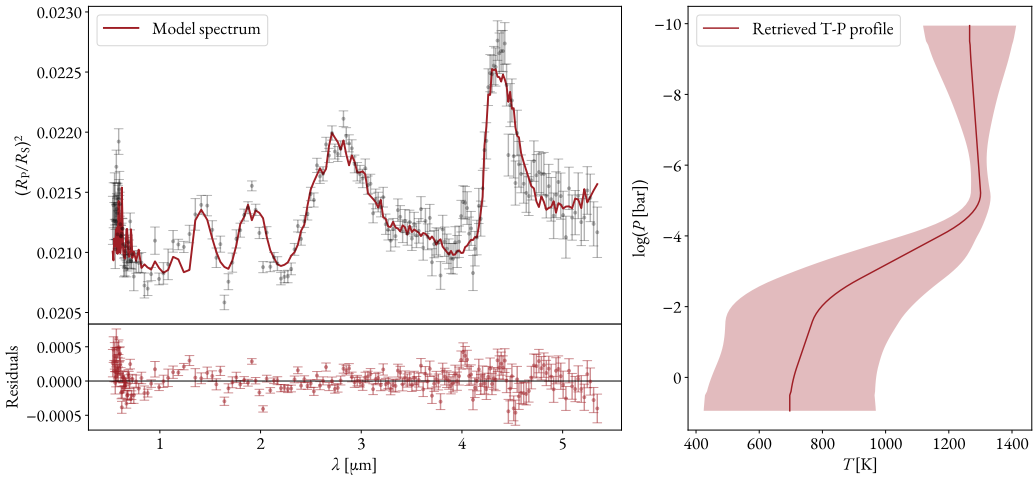

Figure 4.4: Fitted spectrum (left) and temperature-pressure profile (right) of Model 4. This model fits the He/H_2 ratio and includes CIA.

To try to better fit the lower-wavelength parts of the spectrum, Model 6 was created by removing TiO and VO, and adding Na and K, compared to Model 5.

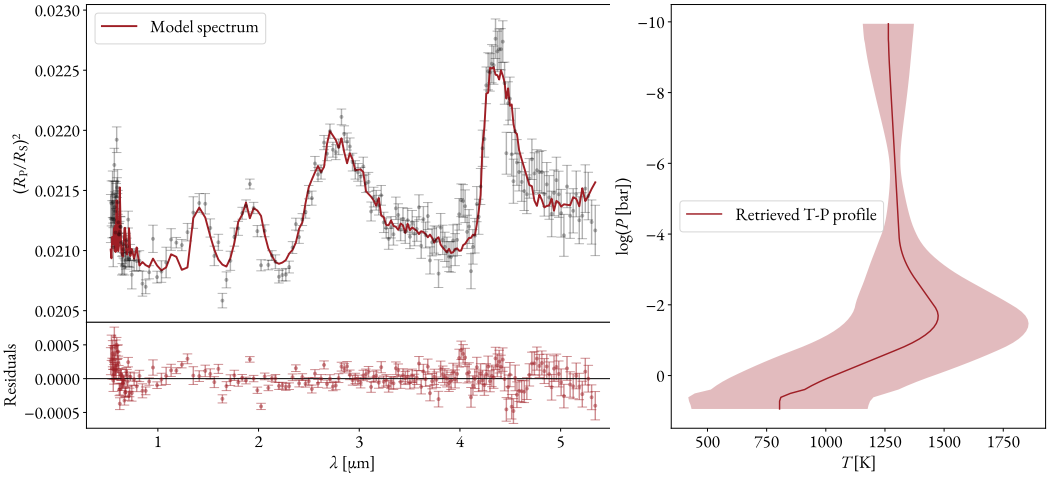

Figure 4.5: Fitted spectrum (left) and temperature-pressure profile (right) of Model 5. This model is the same as Model 4 but does not fit the He/H_2 ratio.

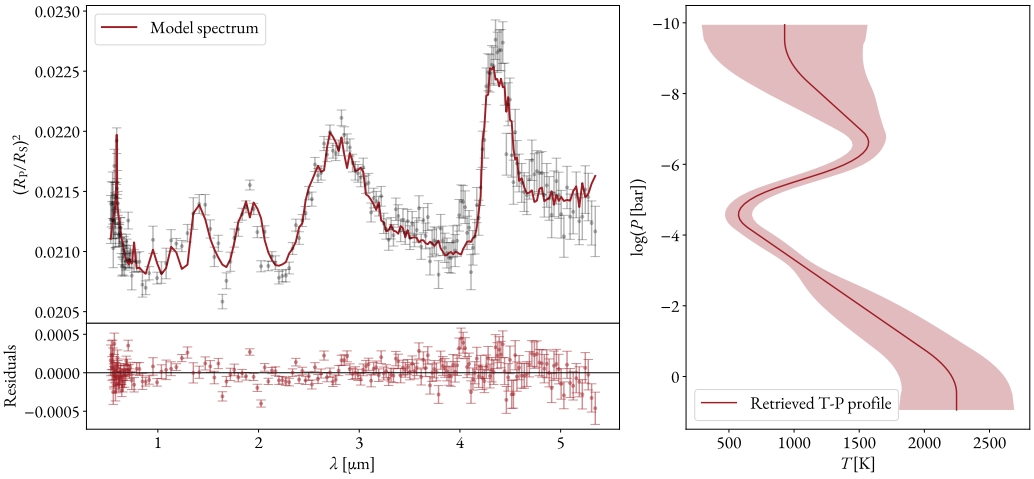

Figure 4.6: Fitted spectrum (left) and temperature-pressure profile (right) of Model 6. This model is the same as Models 4 and 5, but instead of TiO and VO it uses Na and K.

Figure 3.1 shows an anomaly around 4μm. This absorption feature could indicate the presence of SO_2 [7], therefore SO_2 was added as an absorbing species in Model 7, K was removed, and TiO and VO were put back. Otherwise, this model was unchanged compared to Model 6. This, however resulted in a best-fit T-P profile that had a very low temperature in the deep regions of the planet, which is not expected considering WASP-39b is a hot Jupiter.

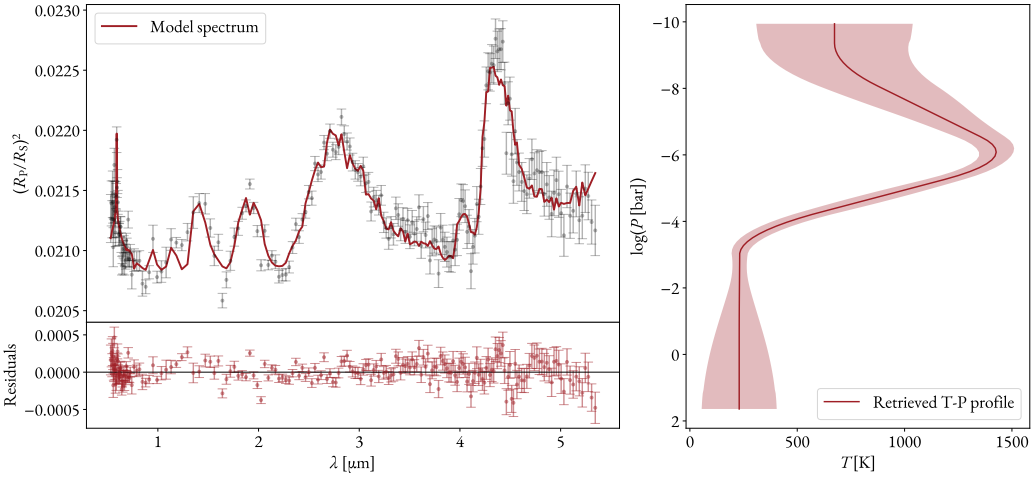

Figure 4.7: Fitted spectrum (left) and temperature-pressure profile (right) of Model 7. This model is the same as Model 6, but it includes SO_2, TiO and VO, and excludes K.

Considering this, another model was created (Model 8), only changing the prior surface temperature ranges to try to constrain it between more expected values (that is, between 1500K and 3500K).

Afterwards, a model identical to Model 7 was created, but excluding CIA. The motivation behind this was to check the statistical contribution of CIA in the models. This is Model 9.

To check again whether the Guillot 2010 T-P profile is a better fit than a 4-point one, two additional models were created (one with, and one without CIA), these being Model 10 and Model 11. They are otherwise the same as Model 7, except in their T-P profile.

One-dimensional model with equilibrium chemistry

Apart from all the previous models, which had a free chemistry, a model with equilibrium chemistry was created (Model 12), fitting the C/O ratio. This model also assumes 4 T-P points. It was used to asses whether the planet is more likely in chemical equilibrium or in chemical disequilibrium.

4.2.2 Two-dimensional models

From the models of Carone et al. 2023 [11] it is likely that the planet shows differences between its day and night sides, that can affect the transmission spectrum. Falco et al. [17], Pluriel et al. [18], and Zingales et al. [19] showed that the atmospheric parameters may be biased if they are retrieved using a one-dimensional assumption. For this reason, some two-dimensional models were created. They have three different (deep, day and night) values for the chemical species' mixing ratios and for the T-P profiles (compared to the constant ones of all of the 1D models). They also require fitting of the pressure above which the atmosphere is considered uniform across the whole planet (P_{iso}), as well as (β), which defines the day-night terminator area. These are Models 1-

2D and 2-2D, and they use the chemical composition of Model 7. Their spectra can be seen in Figure 4.8 and Figure 4.9, respectively.

The difference between these two models is that Model 1-2D does not take into account the dissociation of H_2 and H_2O, while Model 2-2D does.

These models are otherwise the same as Model 7, but considering every additional absorbing species means three additional fitting parameters, the T-P profile was limited to being isothermal in all three "layers", as having a 4-point profile would require fitting 9 more parameters. Taking computational cost into account, and the already quite high number of parameters (28), a decision was made against using a 4-point profile.

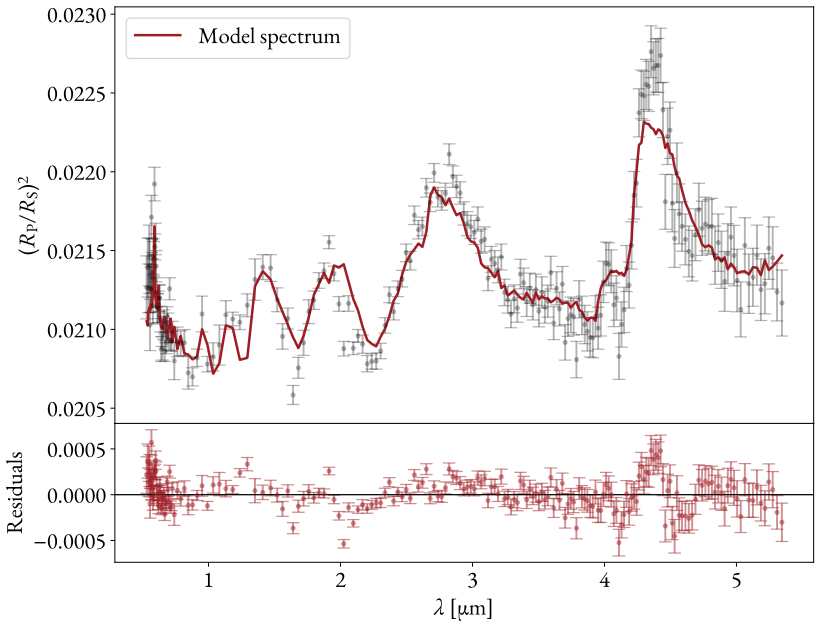

Figure 4.8: Fitted spectrum of Model 1-2D. This model does not take into account the photodissociation of H_2O and H_2.

4.2.3 Model comparison

All the models discussed in the previous subsection are summarized in Table 4.2. The main method for the comparison of models was the Bayes factor, discussed in section 3.5. Judging by this criterion, Model 6 is the one that best describes this spectrum, and is therefore used as a reference point for calculating the Bayes factor between models. This model does not include SO_2 as an absorbing species. It was in any case assessed that SO_2 is likely present in the atmosphere, because it is the only species that can fit the bump in the spectrum at around 4μm. The likely reason for the evidence of Model 6 being higher than that of Model 7 is the non-inclusion of K as an absorber in the latter. Other species assessed to be present are CO_2, H_2O, CO, H_2S, Na and K. Models 6,

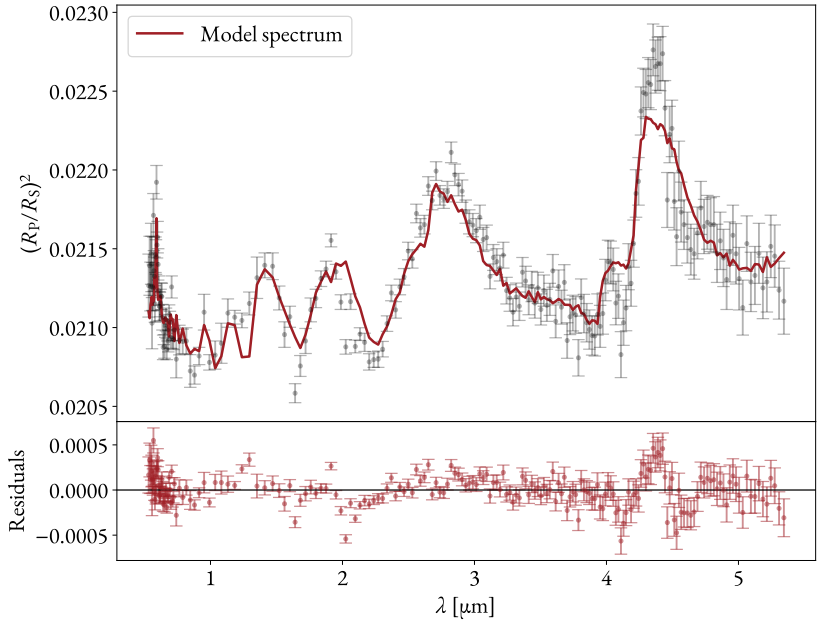

Figure 4.9: Fitted spectrum Model 2-2**D.** This model takes into account the photodissociation of H_2O and H_2, but is otherwise the same as Model 1-2D.

7, and 2-2D, are compared in Figure 4.11. Here, a peak in the residuals for the model without SO_2 in the region around 4μm.

Considering the Bayesian evidences, all 1D models are a better fit than the 2D ones. This is also confirmed by the Bayes factor of any 1D model compared to any 2D one. This could lead to a conclusion that there are no observable day-night differences in the atmosphere, but other possible reasons for these models being a worse fit will be discussed further in section 5.1.

All of the free chemistry models outperform the model with equilibrium chemistry (Model 12) by a very large margin, judging by the log-evidences. This means that it is extremely likely that the planet is not in chemical equilibrium.

Comparing Models 8 and 9 to Models 10 and 11 it can be argued that a 4-point temperature-pressure profile is a much better fit for this exoplanet, when compared to a Guillot 2010 profile. The same can be concluded from the comparison of Models 1 and 2.

The two 2D models are compared in Figure 4.12. Their log-evidences are the same, and they are visually extremely similar. Considering one of them takes the dissociation of H_2 and H_2O into account, and the other does not, it can be said that the findings of this dissociation in the atmosphere are inconclusive.

All of the models have spikes in their residuals in the highest and lowest wavelength ranges, while the 2D models also miss the highest points between 4μm and 5μm. Possible reasons for this will be discussed in section 5.1.

Comparing models with Guillot 2010 temperature-pressure profiles, to similar ones with 4-point profiles (i.e.

comparing Model 1 to Model 2, or Models 7, 8 and 9 to Models 10 and 11), it is certain that a 4-point temperature profile is a better choice. All of the models with a 4-point profile exhibit a distinct thermal inversion (e.g. Figure 4.10).

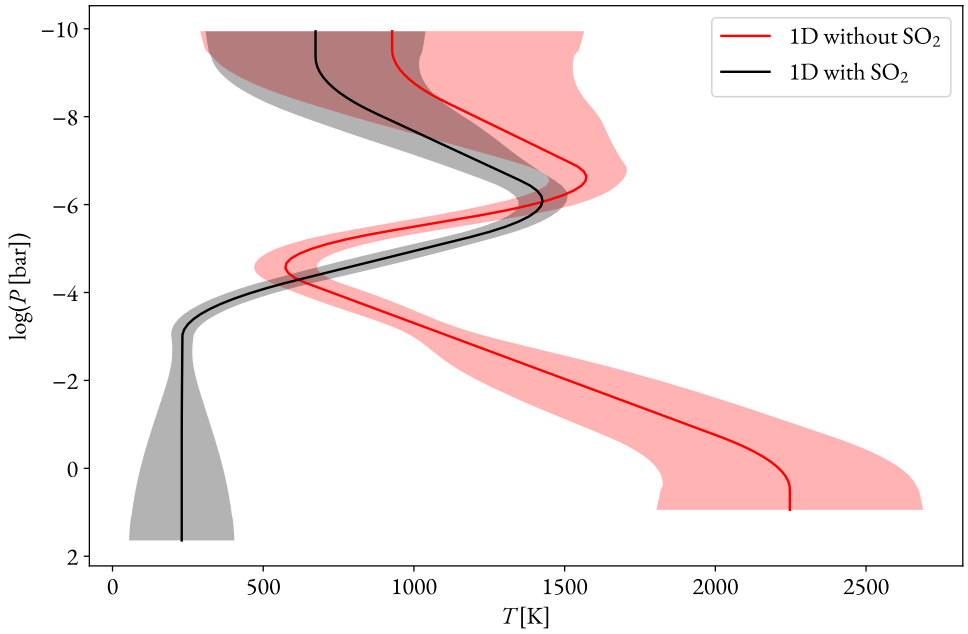

Figure 4.10: Comparison between the temperature-pressure profiles of a 1D model with (Model 7) and without SO_2 (Model 6). It can be seen that both models exhibit a thermal inversion in a similar temperature-pressure region, but the model without SO_2 infers a very low temperature in the deepest regions of the atmosphere.

Table 4.2: Compared models and their log-Bayes factors with respect to Model 6. This model had the highest Bayesian log-evidence and is therefore used as a reference point. A value closer to zero translates to a better fit. The two-dimensional models have a note specifying whether or not the photodissociation of H_2 and H_2O was taken into consideration, while the one-dimensional models do not include photodissociation.

i	Model type	Chemistry	T-P profile	Chemical species	Note	$\log(B_{i6})$
1	1D	free	Guillot 2010	CO_2, CO, H_2O, TiO	no CIA, He/H_2 fitted	-91.6 ± 0.3
2			4-point	CO_2, CO, H_2O, TiO	no CIA, He/H_2 fitted	-80.0 ± 0.1
3			4-point	CO_2, CO, H_2O, TiO, VO	He/H_2 fitted	-155.2 ± 0.3
4		free	4-point	CO_2, CO, H_2O, H_2S, TiO, VO	He/H_2 fitted	-105.0 ± 0.3
5				CO_2, CO, H_2O, H_2S, TiO, VO		-103.4 ± 0.3
6				CO_2, CO, H_2O, H_2S, Na, K		0.0 ± 0.2
7				CO_2, CO, H_2O, H_2S, Na, TiO, VO, SO_2		-25.4 ± 0.2
8		free	4-point	CO_2, CO, H_2O, H_2S, Na, TiO, VO, SO_2	T constrained	-29.9 ± 0.3
9			4-point		no CIA	-24.6 ± 0.3
10			Guillot 2010			-195.0 ± 0.3
11			Guillot 2010		no CIA	-144.7 ± 0.3
12		equilibrium	4-point	N/A (C/O ratio fitted)		-212.0 ± 0.2
1-2D	2D	free	isothermal	CO_2, CO, H_2O, H_2S, Na, TiO, VO, SO_2	no dissociation	-201.2 ± 0.3
2-2D					w/ dissociation	-201.1 ± 0.3

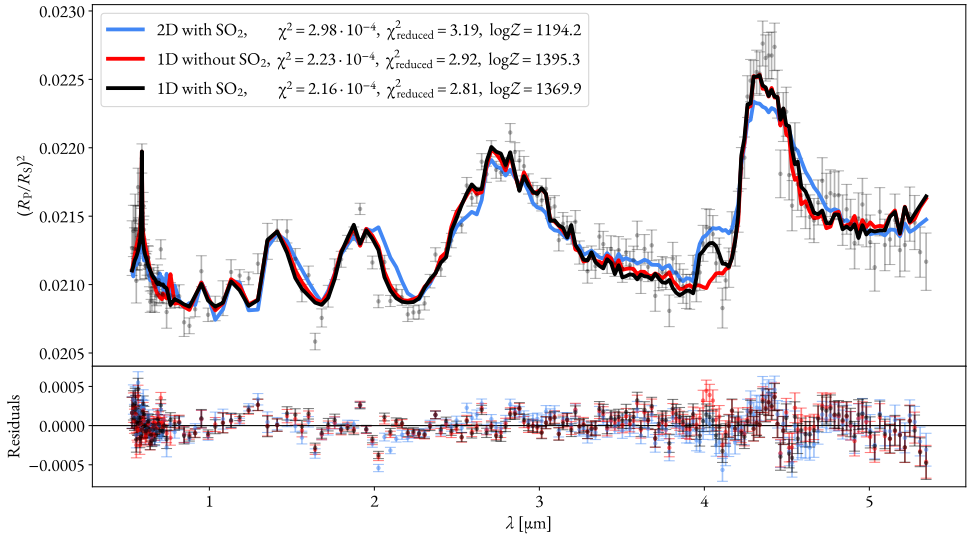

Figure 4.11: Comparison between 1D models with/without SO_2 and a 2D model with SO_2 and photodissociation. The legend shows the χ^2 and log-evidence values for each of the models. (blue line - Model 2-2D, red line - Model 6, black line - Model 7)

4.3 Parameter solutions

The values of the parameters fitted from 1D models are presented in Table 4.3 (Model 6) and Table 4.4 (Model 7), while the ones from the 2D models can be seen in Table 4.5. Model 6 is the best-fit model. Model 7 is included here to illustrate the detection of SO_2 and non-detection or weak detection of TiO and VO. Notable is the high mean molecular weight in the 1D models, and even higher so in the 2D ones, as well as the very high mixing ratio of sodium (Na).

The 2D model parameter solutions are all from the model with H_2O dissociation turned on, because this dissociation is expected in the temperature and pressure ranges of this planetary atmosphere. Some peculiarities here are the overlapping values for the temperatures on the day and night sides, which suggest either no, or negligible day-night differences. This is not to say that these differences do not exist, especially so because of the large uncertainties of the inferred day and night temperatures.

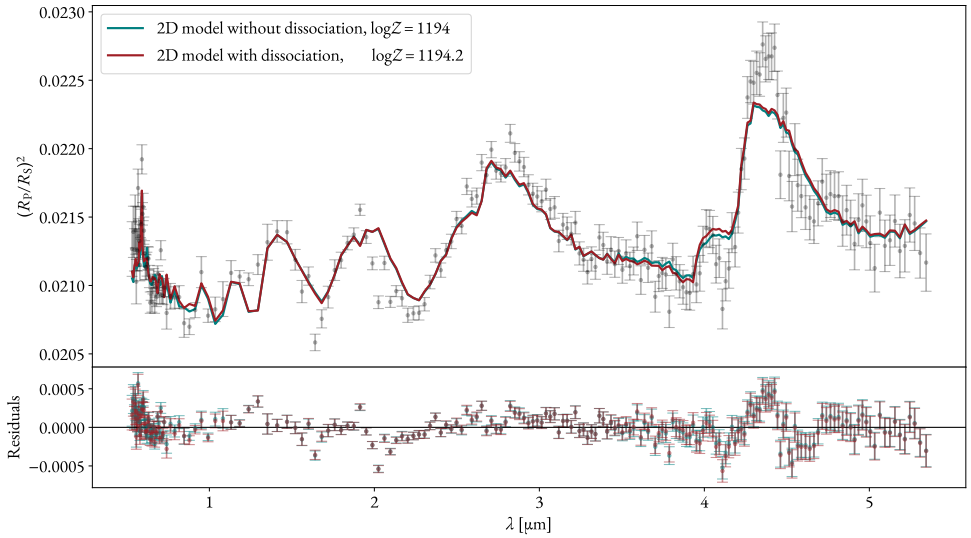

Figure 4.12: Comparison between 2D models with and without H_2 and H_2O photodissociation. It can be seen that the models are very close to each other. The legend shows the log-evidence values for each of the two models.

Table 4.3: Model 6: Fitted 1D model parameters and their values. This model uses Na and K instead of TiO and VO as absorbers in the optical wavelength range. This is the model with the highest log-evidence.

Parameter	Value
R_P [R_J]	1.21 ± 0.02
T_s [K]	2218 ± 497
T_1 [K]	549 ± 159
T_2 [K]	1670 ± 265
T_t [K]	1046 ± 537
$\log(P_\mathrm{clouds}$ [bar])	-3.24 ± 0.16
$\log(P_s$ [bar])	-0.9 ± 1.2
$\log(P_1$ [bar])	-5.4 ± 0.5
$\log(P_2$ [bar])	-6.4 ± 1.1
$\log(P_t$ [bar])	-8.9 ± 1.3
CO mixing ratio	$(2.3 \pm 1.1) \times 10^{-2}$
CO_2 mixing ratio	$(8 \pm 3) \times 10^{-4}$
H_2O mixing ratio	$(3.9 \pm 1.0) \times 10^{-2}$
H_2S mixing ratio	$(3.5 \pm 0.9) \times 10^{-3}$
Na mixing ratio	$(3.1 \pm 1.3) \times 10^{-2}$
K mixing ratio	$(1.6 \pm 0.8) \times 10^{-4}$
μ	4.3 ± 0.3

Table 4.4: Model 7: Fitted 1D model parameters and their values. This model adds SO_2, omits K and additionally uses TiO and VO as absorbers in the optical wavelength range.

Parameter	Value
R_P [R_J]	1.303 ± 0.008
T_s [K]	291 ± 211
T_1 [K]	312 ± 295
T_2 [K]	1558 ± 138
T_t [K]	696 ± 393
$\log(P_\mathrm{clouds}$ [bar])	-0.6 ± 1.1
$\log(P_s$ [bar])	-1.0 ± 2.1
$\log(P_1$ [bar])	-3.8 ± 1.0
$\log(P_2$ [bar])	-5.9 ± 0.5
$\log(P_t$ [bar])	-8.7 ± 1.4
CO mixing ratio	$(2.0 \pm 0.8) \times 10^{-2}$
CO_2 mixing ratio	$(6 \pm 2) \times 10^{-4}$
H_2O mixing ratio	$(3.6 \pm 0.8) \times 10^{-2}$
H_2S mixing ratio	$(3 \pm 1) \times 10^{-3}$
Na mixing ratio	$(3.5 \pm 1.1) \times 10^{-2}$
SO_2 mixing ratio	$(1.2 \pm 0.4) \times 10^{-4}$
TiO mixing ratio	$(1.1 \pm 0.5) \times 10^{-9}$
VO mixing ratio	$(5.9 \pm 3.1) \times 10^{-9}$
μ	4.3 ± 0.4

Table 4.5: Fitted 2D model parameters and their values. Taken from the 2D model with H_2 and H_2O dissociation included. (Model $2-2D$)

Parameter	Value
$R_P\,[R_J]$	1.275 ± 0.002
$T_{day}\,[K]$	1230 ± 530
$T_{night}\,[K]$	1010 ± 500
$T_{deep}\,[K]$	1162 ± 25
$\log(P_{iso}\,[bar])$	1.62 ± 0.20
$\log(P_{clouds,\,day}\,[bar])$	0.73 ± 0.31
$\log(P_{clouds,\,night}\,[bar])$	0.76 ± 0.29
CO^{day} mixing ratio	0.062 ± 0.018
CO^{night} mixing ratio	0.027 ± 0.013
CO^{deep} mixing ratio	0.082 ± 0.008
$CO_2{}^{day}$ mixing ratio	0.035 ± 0.016
$CO_2{}^{night}$ mixing ratio	0.041 ± 0.015
$CO_2{}^{deep}$ mixing ratio	0.0164 ± 0.0023
H_2O^{day} mixing ratio	0.033 ± 0.015
H_2O^{night} mixing ratio	0.040 ± 0.022
H_2O^{deep} mixing ratio	0.060 ± 0.0063
H_2S^{day} mixing ratio	0.039 ± 0.016
H_2S^{night} mixing ratio	0.070 ± 0.014
H_2S^{deep} mixing ratio	0.0058 ± 0.0014
Na^{day} mixing ratio	0.050 ± 0.018
Na^{night} mixing ratio	0.047 ± 0.018
Na^{deep} mixing ratio	0.070 ± 0.007
$SO_2{}^{day}$ mixing ratio	0.067 ± 0.015
$SO_2{}^{night}$ mixing ratio	0.064 ± 0.015
$SO_2{}^{deep}$ mixing ratio	0.0011 ± 0.0008
TiO^{day} mixing ratio	0.060 ± 0.019
TiO^{night} mixing ratio	0.075 ± 0.011
TiO^{deep} mixing ratio	$(1.94 \pm 1.52) \times 10^{-8}$
VO^{day} mixing ratio	0.045 ± 0.017
VO^{night} mixing ratio	0.053 ± 0.020
VO^{deep} mixing ratio	$(9.75 \pm 3.55) \times 10^{-8}$
μ	7.51 ± 0.12
$\beta\,[^\circ]$	23.3 ± 3.8

5 Discussion and conclusion

5.1 Discussion

While a number of conclusions can be drawn from the results exponed in chapter 4, multiple things remain uncertain and unsolved.

One of the issues is the uncertainty of the fitting of the limiting wavelength regions. For the lower wavelength regions, among the currently tested models, sodium (Na) seems to be the best-fitting absorber. However, the high mixing ratios of sodium required to fit this absorption do not seem realistic, as the mixing ratio required is of the order of that of water, which is generally a much more common chemical species. I would not exclude the possibility of having a high mixing ratio of sodium in the probed atmospheric regions, but would still consider it unlikely. Even though sodium is the best solution among the ones tested, the residuals still have a spike at the lowest wavelengths, which probably means there is another explanation for the behaviour of the spectrum in this region. The reasons could also likely be linked to the instrumental sensitivity and/or noise.

As for the highest wavelength regions, the absorption here is usually overestimated by the models. A solution to this could be to use more complex stellar models (e.g. PHOENIX), instead of a simple black body model. This should be tested in future work.

The high inferred value of the mean molecular weight μ should also be taken with a grain of salt. Line & Parmentier 2016 [16] find a degeneracy between a patchy cloud coverage and a high mean molecular weight. Considering all the models in this work assumed simple clouds, this could be a possible reason for the very high inferred μ. A higher μ value would in turn require a higher-than-solar metallicity, which would require an explanation, considering the star in question is a solar-type star, and has a metallicity close to the solar one. This being considered, an improvement to the models created could be a more complex cloud model - which would enable also checking whether or not that would influence the μ value in this particular case.
It should, however, be emphasized, that Carone et al. 2023 [11], with GCMs, found multiple possible solutions

for the value of μ, one of them being in agreement with the one found in this work. This finding therefore still has some backing.

Although the day-night differences inferred from this spectrum do not seem to be significant (Table 4.5), there have been recent observational findings (Espinoza et al. 2024 [12]), as well as models (Carone et al. 2023) that have found and constrained these differences. The possible reasons for their non-detection in this work might be the oversimplified temperature-pressure profiles used in the 2D models in this work. These differences could be possibly found if more complex T-P profiles had been used.

The mixing ratio profiles used in the 1D models in this work are all simple (i.e. they are constant throughout the atmosphere). This is not very realistic, considering the different weights of the different molecules, and considering the findings from the 2D models, where some significant differences have been found between the mixing ratios in the deep and day/night layers (Table 4.5, especially TiO, VO, SO_2). Switching to a two-level profile could possibly improve the one-dimensional models further.

The non-detection of CH_4 could also not be accurate, as this molecule is usually found in the lower regions of atmospheres, and considering the high inflation of this particular atmosphere, it could be that the CH_4 in this atmosphere is simply hidden by its cloud layer.

The inconclusiveness of the photodissociation of H_2 and H_2O should also be further explored, as the temperatures and pressures of a planet like WASP-39b should be sufficient for this dissociation to occur. If there is no dissociation, then there could be an unknown mechanism preventing this from occurring, which should in any case be of research interest.

5.2 Conclusion

Exoplanet characterization has been one of the main goals of exoplanet science since its beginnings. Hot Jupiters, being the most commonly observed exoplanets, are in the focus of this field. This is especially because, with current instruments, they are the ones which we can infer the most details about. The analysis of the atmospheres of exoplanets reveals a large amount of information on their chemical compositions and temperature-pressure profiles.

In this work, I summarized the current findings about the atmosphere of WASP-39b and similar exoplanetary atmospheres. I explained the principles of transmission spectroscopy, the theory of spectral line formation, absorption in planetary atmospheres as well as other mechanisms such as scattering and collision-induced absorption, which are most significant for the spectra of planetary atmospheres. All of these mechanisms have then been connected together through the principles of radiative transfer, which is at the core of atmospheric modelling.

The work revolves around an inverse forward modelling approach, which was used to infer the atmospheric parameters. This makes use of the TauREx and TauREx-2D retrieval frameworks, FastChem and the MultiNest sampler, to create different forward models and then retrieve the best-fit parameter values of these models for this spectrum, from set priors.

A number of models of varying complexity were created, ranging from one-dimensional isothermal models with free chemistry, through models with 4-point temperature-pressure profiles, models with equilibrium chemistry and, the most complex, two-dimensional models. Among these, the Bayes factor was used to pick the best models, and from the ones chosen, the values of the atmospheric parameters were concluded, these being plane-

tary radius, atmospheric temperature-pressure profile, chemical species mixing ratios and mean molecular weight.

I conclude that one-dimensional models are likely sufficient for modelling this specific spectrum of WASP-39b. This means that day-night differences have not been detected, which is in conflict with other works (that make use of additional observations), that have found these differences.

The results very strongly indicate that the planet is not in chemical equilibrium. The Bayes factor between the models without and with chemical equilibrium translates to a 20σ significance in favour of the models with disequilibrium chemistry . This is a crucial finding, as it is in support of an atmosphere with active and ongoing photochemical processes, atmospheric mixing, or possibly other, unexplained processes. The detected presence of SO_2 also points towards chemical disequilibrium - i.e. these two findings are in support of each other. The high mean molecular weight (μ) detected, under the assumption of simple clouds, is also of significance.

A thermal inversion appears to be a consistent feature across most models, which is a common feature for an atmosphere with absorbers in the optical wavelength range.

Detections of CO_2, H_2O, CO, H_2S, SO_2, Na, and K are quite likely, and in line with other works (e.g. Rustamkulov et al. 2023 [7]) as well as the found very weak detections or non-detections of TiO, VO, and CH_4. The potential dissociation of H_2O and H_2 remains uncertain and requires further analysis.

An unexpected temperature-pressure (T-P) profile is found in some of the one-dimensional models, particularly in those with SO_2, TiO and VO. This anomaly highlights the need for additional research to fully understand the complexities of this planetary atmosphere.

References

[1] M. Mayor and D. Queloz, "A Jupiter-mass companion to a solar-type star," *Nature*, vol. 378, no. 6555, pp. 355–359, Nov. 1995.

[2] A. H. M. J. Triaud, J. de Wit, F. Klein, M. Turbet, B. V. Rackham, P. Niraula, A. Glidden, O. E. Jagoutz, M. Peč, J. J. Petkowski, S. Seager, and F. Selsis, "Atmospheric carbon depletion as a tracer of water oceans and biomass on temperate terrestrial exoplanets," *Nature Astronomy*, Dec. 2023.

[3] F. Faedi, S. C. C. Barros, D. R. Anderson, D. J. A. Brown, A. Collier Cameron, D. Pollacco, I. Boisse, G. Hébrard, M. Lendl, T. A. Lister, B. Smalley, R. A. Street, A. H. M. J. Triaud, J. Bento, F. Bouchy, O. W. Butters, B. Enoch, C. A. Haswell, C. Hellier, F. P. Keenan, G. R. M. Miller, V. Moulds, C. Moutou, A. J. Norton, D. Queloz, A. Santerne, E. K. Simpson, I. Skillen, A. M. S. Smith, S. Udry, C. A. Watson, R. G. West, and P. J. Wheatley, "WASP-39b: a highly inflated Saturn-mass planet orbiting a late G-type star," *Astronomy and Astrophysics*, vol. 531, p. A40, Jul. 2011.

[4] R. A. Street, D. L. Pollaco, A. Fitzsimmons, F. P. Keenan, K. Horne, S. Kane, A. Collier Cameron, T. A. Lister, C. Haswell, A. J. Norton, B. W. Jones, I. Skillen, S. Hodgkin, P. Wheatley, R. West, and D. Brett, "SuperWASP: Wide Angle Search for Planets," in *Scientific Frontiers in Research on Extrasolar Planets*, ser. Astronomical Society of the Pacific Conference Series, D. Deming and S. Seager, Eds., vol. 294, Jan. 2003, pp. 405–408.

[5] H. R. Wakeford, D. K. Sing, D. Deming, N. K. Lewis, J. Goyal, T. J. Wilson, J. Barstow, T. Kataria, B. Drummond, T. M. Evans, A. L. Carter, N. Nikolov, H. A. Knutson, G. E. Ballester, and A. M. Mandell, "The Complete Transmission Spectrum of WASP-39b with a Precise Water Constraint," *Astronomical Journal*, vol. 155, no. 1, p. 29, Jan. 2018.

[6] JWST Transiting Exoplanet Community Early Release Science Team, E.-M. Ahrer, L. Alderson, N. M. Batalha, N. E. Batalha, J. L. Bean, T. G. Beatty, T. J. Bell, B. Benneke, Z. K. Berta-Thompson, A. L. Carter, I. J. M. Crossfield, N. Espinoza, A. D. Feinstein, J. J. Fortney, N. P. Gibson, J. M. Goyal, E. M. R. Kempton, J. Kirk, L. Kreidberg, M. López-Morales, M. R. Line, J. D. Lothringer, S. E. Moran, S. Mukherjee, K. Ohno, V. Parmentier, C. Piaulet, Z. Rustamkulov, E. Schlawin, D. K. Sing, K. B. Stevenson, H. R. Wakeford, N. H. Allen, S. M. Birkmann, J. Brande, N. Crouzet, P. E. Cubillos, M. Damiano, J.-M. Désert, P. Gao, J. Harrington, R. Hu, S. Kendrew, H. A. Knutson, P.-O. Lagage, J. Leconte, M. Lendl, R. J. MacDonald, E. M. May, Y. Miguel, K. Molaverdikhani, J. I. Moses, C. A. Murray, M. Nehring, N. K. Nikolov, D. J. M. Petit dit de la Roche, M. Radica, P.-A. Roy, K. G. Stassun, J. Taylor, W. C. Waalkes, P. Wachiraphan, L. Welbanks, P. J. Wheatley, K. Aggarwal, M. K. Alam, A. Banerjee, J. K. Barstow, J. Blecic, S. L. Casewell, Q. Changeat, K. L. Chubb, K. D. Colón, L.-P. Coulombe, T. Daylan, M. de Val-Borro, L. Decin, L. A. Dos Santos, L. Flagg, K. France, G. Fu, A. García Muñoz, J. E. Gizis, A. Glidden, D. Grant, K. Heng, T. Henning, Y.-C. Hong, J. Inglis, N. Iro, T. Kataria, T. D. Komacek, J. E. Krick, E. K. H. Lee, N. K.

Lewis, J. Lillo-Box, J. Lustig-Yaeger, L. Mancini, A. M. Mandell, M. Mansfield, M. S. Marley, T. Mikal-Evans, G. Morello, M. C. Nixon, K. Ortiz Ceballos, A. A. A. Piette, D. Powell, B. V. Rackham, L. Ramos-Rosado, E. Rauscher, S. Redfield, L. K. Rogers, M. T. Roman, G. M. Roudier, N. Scarsdale, E. L. Shkolnik, J. Southworth, J. J. Spake, M. E. Steinrueck, X. Tan, J. K. Teske, P. Tremblin, S.-M. Tsai, G. S. Tucker, J. D. Turner, J. A. Valenti, O. Venot, I. P. Waldmann, N. L. Wallack, X. Zhang, and S. Zieba, "Identification of carbon dioxide in an exoplanet atmosphere," *Nature*, vol. 614, no. 7949, pp. 649–652, Feb. 2023.

[7] Z. Rustamkulov, D. K. Sing, S. Mukherjee, E. M. May, J. Kirk, E. Schlawin, M. R. Line, C. Piaulet, A. L. Carter, N. E. Batalha, J. M. Goyal, M. López-Morales, J. D. Lothringer, R. J. MacDonald, S. E. Moran, K. B. Stevenson, H. R. Wakeford, N. Espinoza, J. L. Bean, N. M. Batalha, B. Benneke, Z. K. Berta-Thompson, I. J. M. Crossfield, P. Gao, L. Kreidberg, D. K. Powell, P. E. Cubillos, N. P. Gibson, J. Leconte, K. Molaverdikhani, N. K. Nikolov, V. Parmentier, P. Roy, J. Taylor, J. D. Turner, P. J. Wheatley, K. Aggarwal, E. Ahrer, M. K. Alam, L. Alderson, N. H. Allen, A. Banerjee, S. Barat, D. Barrado, J. K. Barstow, T. J. Bell, J. Blecic, J. Brande, S. Casewell, Q. Changeat, K. L. Chubb, N. Crouzet, T. Daylan, L. Decin, J. Désert, T. Mikal-Evans, A. D. Feinstein, L. Flagg, J. J. Fortney, J. Harrington, K. Heng, Y. Hong, R. Hu, N. Iro, T. Kataria, E. M. R. Kempton, J. Krick, M. Lendl, J. Lillo-Box, A. Louca, J. Lustig-Yaeger, L. Mancini, M. Mansfield, N. J. Mayne, Y. Miguel, G. Morello, K. Ohno, E. Palle, D. J. M. Petit dit de la Roche, B. V. Rackham, M. Radica, L. Ramos-Rosado, S. Redfield, L. K. Rogers, E. L. Shkolnik, J. Southworth, J. Teske, P. Tremblin, G. S. Tucker, O. Venot, W. C. Waalkes, L. Welbanks, X. Zhang, and S. Zieba, "Early Release Science of the exoplanet WASP-39b with JWST NIRSpec PRISM," *Nature*, vol. 614, no. 7949, pp. 659–663, Feb. 2023.

[8] S.-M. Tsai, E. K. H. Lee, D. Powell, P. Gao, X. Zhang, J. Moses, E. Hébrard, O. Venot, V. Parmentier, S. Jordan, R. Hu, M. K. Alam, L. Alderson, N. M. Batalha, J. L. Bean, B. Benneke, C. J. Bierson, R. P. Brady, L. Carone, A. L. Carter, K. L. Chubb, J. Inglis, J. Leconte, M. Line, M. López-Morales, Y. Miguel, K. Molaverdikhani, Z. Rustamkulov, D. K. Sing, K. B. Stevenson, H. R. Wakeford, J. Yang, K. Aggarwal, R. Baeyens, S. Barat, M. de Val-Borro, T. Daylan, J. J. Fortney, K. France, J. M. Goyal, D. Grant, J. Kirk, L. Kreidberg, A. Louca, S. E. Moran, S. Mukherjee, E. Nasedkin, K. Ohno, B. V. Rackham, S. Redfield, J. Taylor, P. Tremblin, C. Visscher, N. L. Wallack, L. Welbanks, A. Youngblood, E.-M. Ahrer, N. E. Batalha, P. Behr, Z. K. Berta-Thompson, J. Blecic, S. L. Casewell, I. J. M. Crossfield, N. Crouzet, P. E. Cubillos, L. Decin, J.-M. Désert, A. D. Feinstein, N. P. Gibson, J. Harrington, K. Heng, T. Henning, E. M. R. Kempton, J. Krick, P.-O. Lagage, M. Lendl, J. D. Lothringer, M. Mansfield, N. J. Mayne, T. Mikal-Evans, E. Palle, E. Schlawin, O. Shorttle, P. J. Wheatley, and S. N. Yurchenko, "Photochemically produced SO_2 in the atmosphere of WASP-39b," *Nature*, vol. 617, no. 7961, pp. 483–487, May 2023.

[9] D. Powell, A. D. Feinstein, E. K. H. Lee, M. Zhang, S.-M. Tsai, J. Taylor, J. Kirk, T. Bell, J. K. Barstow, P. Gao, J. L. Bean, J. Blecic, K. L. Chubb, I. J. M. Crossfield, S. Jordan, D. Kitzmann, S. E. Moran, G. Morello, J. I. Moses, L. Welbanks, J. Yang, X. Zhang, E.-M. Ahrer, A. Bello-Arufe, J. Brande, S. L. Casewell, N. Crouzet, P. E. Cubillos, B.-O. Demory, A. Dyrek, L. Flagg, R. Hu, J. Inglis, K. D. Jones, L. Kreidberg, M. López-Morales, P.-O. Lagage, E. A. Meier Valdés, Y. Miguel, V. Parmentier, A. A. A. Piette, B. V. Rackham, M. Radica, S. Redfield, K. B. Stevenson, H. R. Wakeford, K. Aggarwal, M. K. Alam, N. M. Batalha, N. E. Batalha, B. Benneke, Z. K. Berta-Thompson, R. P. Brady, C. Caceres, A. L. Carter, J.-M. Désert, J. Harrington, N. Iro, M. R. Line, J. D. Lothringer, R. J. MacDonald, L. Mancini,

K. Molaverdikhani, S. Mukherjee, M. C. Nixon, A. V. Oza, E. Palle, Z. Rustamkulov, D. K. Sing, M. E. Steinrueck, O. Venot, P. J. Wheatley, and S. N. Yurchenko, "Sulfur dioxide in the mid-infrared transmission spectrum of WASP-39b," *Nature*, vol. 626, no. 8001, pp. 979–983, Feb. 2024.

[10] Y. Kawashima and M. Min, "Implementation of disequilibrium chemistry to spectral retrieval code ARCiS and application to 16 exoplanet transmission spectra. Indication of disequilibrium chemistry for HD 209458b and WASP-39b," *Astronomy and Astrophysics*, vol. 656, p. A90, Dec. 2021.

[11] L. Carone, D. A. Lewis, D. Samra, A. D. Schneider, and C. Helling, "WASP-39b: exo-Saturn with patchy cloud composition, moderate metallicity, and underdepleted S/O," *arXiv e-prints*, p. arXiv:2301.08492, Jan. 2023.

[12] N. Espinoza, M. E. Steinrueck, J. Kirk, R. J. MacDonald, A. B. Savel, K. Arnold, E. M. R. Kempton, M. M. Murphy, L. Carone, M. Zamyatina, D. A. Lewis, D. Samra, S. Kiefer, E. Rauscher, D. Christie, N. Mayne, C. Helling, Z. Rustamkulov, V. Parmentier, E. M. May, A. L. Carter, X. Zhang, M. López-Morales, N. Allen, J. Blecic, L. Decin, L. Mancini, K. Molaverdikhani, B. V. Rackham, E. Palle, S.-M. Tsai, E.-M. Ahrer, J. L. Bean, I. J. M. Crossfield, D. Haegele, E. Hébrard, L. Kreidberg, D. Powell, A. D. Schneider, L. Welbanks, P. Wheatley, R. Brahm, and N. Crouzet, "Inhomogeneous terminators on the exoplanet WASP-39 b," *arXiv e-prints*, p. arXiv:2407.10294, Jul. 2024.

[13] T. J. Bell, N. Crouzet, P. E. Cubillos, L. Kreidberg, A. A. A. Piette, M. T. Roman, J. K. Barstow, J. Blecic, L. Carone, L.-P. Coulombe, E. Ducrot, M. Hammond, J. M. Mendonça, J. I. Moses, V. Parmentier, K. B. Stevenson, L. Teinturier, M. Zhang, N. M. Batalha, J. L. Bean, B. Benneke, B. Charnay, K. L. Chubb, B.-O. Demory, P. Gao, E. K. H. Lee, M. López-Morales, G. Morello, E. Rauscher, D. K. Sing, X. Tan, O. Venot, H. R. Wakeford, K. Aggarwal, E.-M. Ahrer, M. K. Alam, R. Baeyens, D. Barrado, C. Caceres, A. L. Carter, S. L. Casewell, R. C. Challener, I. J. M. Crossfield, L. Decin, J.-M. Désert, I. Dobbs-Dixon, A. Dyrek, N. Espinoza, A. D. Feinstein, N. P. Gibson, J. Harrington, C. Helling, R. Hu, N. Iro, E. M. R. Kempton, S. Kendrew, T. D. Komacek, J. Krick, P.-O. Lagage, J. Leconte, M. Lendl, N. T. Lewis, J. D. Lothringer, I. Malsky, L. Mancini, M. Mansfield, N. J. Mayne, T. M. Evans-Soma, K. Molaverdikhani, N. K. Nikolov, M. C. Nixon, E. Palle, D. J. M. Petit dit de la Roche, C. Piaulet, D. Powell, B. V. Rackham, A. D. Schneider, M. E. Steinrueck, J. Taylor, L. Welbanks, S. N. Yurchenko, X. Zhang, and S. Zieba, "Nightside clouds and disequilibrium chemistry on the hot Jupiter WASP-43b," *Nature Astronomy*, Apr. 2024.

[14] A. Tsiaras, I. P. Waldmann, T. Zingales, M. Rocchetto, G. Morello, M. Damiano, K. Karpouzas, G. Tinetti, L. K. McKemmish, J. Tennyson, and S. N. Yurchenko, "A Population Study of Gaseous Exoplanets," *Astronomical Journal*, vol. 155, no. 4, p. 156, Apr. 2018.

[15] Parmentier, Vivien, Line, Mike R., Bean, Jacob L., Mansfield, Megan, Kreidberg, Laura, Lupu, Roxana, Visscher, Channon, Désert, Jean-Michel, Fortney, Jonathan J., Deleuil, Magalie, Arcangeli, Jacob, Showman, Adam P., and Marley, Mark S., "From thermal dissociation to condensation in the atmospheres of ultra hot jupiters: Wasp-121b in context," *Astronomy and Astrophysics*, vol. 617, p. A110, 2018. [Online]. Available: https://doi.org/10.1051/0004-6361/201833059

[16] M. R. Line and V. Parmentier, "The Influence of Non-Uniform Cloud Cover on Transit Transmission Spectra," *arXiv e-prints*, p. arXiv:1511.09443, Nov. 2015.

[17] A. Falco, T. Zingales, W. Pluriel, and J. Leconte, "Toward a multidimensional analysis of transmission spectroscopy. I. Computation of transmission spectra using a 1D, 2D, or 3D atmosphere structure," *Astronomy & Astrophysics*, vol. 658, p. A41, Feb. 2022.

[18] W. Pluriel, J. Leconte, V. Parmentier, T. Zingales, A. Falco, F. Selsis, and P. Bordé, "Toward a multidimensional analysis of transmission spectroscopy. II. Day-night-induced biases in retrievals from hot to ultrahot Jupiters," *Astronomy and Astrophysics*, vol. 658, p. A42, Feb. 2022.

[19] T. Zingales, A. Falco, W. Pluriel, and J. Leconte, "Toward a multidimensional analysis of transmission spectroscopy. III. Modeling 2D effects in retrievals with TauREx," *Astronomy and Astrophysics*, vol. 667, p. A13, Nov. 2022.

[20] M. Perryman, *The Exoplanet Handbook*, 2nd ed. Cambridge University Press, 2018.

[21] S. Seager, D. Deming, and J. A. Valenti, "Transiting Exoplanets with JWST," in *Astrophysics in the Next Decade*, ser. Astrophysics and Space Science Proceedings, vol. 10, Jan. 2009, p. 123.

[22] K. Liou, "Chapter 2 - solar radiation at the top of the atmosphere," in *An Introduction to Atmospheric Radiation*, ser. International Geophysics, K. Liou, Ed. Academic Press, 2002, vol. 84, pp. 37–64. [Online]. Available: https://www.sciencedirect.com/science/article/pii/S0074614202800171

[23] C. Foot, *Atomic Physics*, ser. Oxford Master Series in Physics. OUP Oxford, 2005. [Online]. Available: https://books.google.it/books?id=_CoSDAAAQBAJ

[24] K. Liou, "Chapter 1 - fundamentals of radiation for atmospheric applications," in *An Introduction to Atmospheric Radiation*, ser. International Geophysics, K. Liou, Ed. Academic Press, 2002, vol. 84, pp. 1–36. [Online]. Available: https://www.sciencedirect.com/science/article/pii/S007461420280016X

[25] L. Frommhold, *Collision-induced Absorption in Gases*, ser. Cambridge Monographs on Atomic, Molecular and Chemical Physics. Cambridge University Press, 1993. [Online]. Available: https://books.google.it/books?id=EURrf3q38oMC

[26] K. Liou, "Chapter 3 - absorption and scattering of solar radiation in the atmosphere," in *An Introduction to Atmospheric Radiation*, ser. International Geophysics, K. Liou, Ed. Academic Press, 2002, vol. 84, pp. 65–115. [Online]. Available: https://www.sciencedirect.com/science/article/pii/S0074614202800183

[27] A. F. Al-Refaie, Q. Changeat, I. P. Waldmann, and G. Tinetti, "TauREx 3: A Fast, Dynamic, and Extendable Framework for Retrievals," *Astrophysical Journal*, vol. 917, no. 1, p. 37, Aug. 2021.

[28] F. Feroz, M. P. Hobson, and M. Bridges, "MULTINEST: an efficient and robust Bayesian inference tool for cosmology and particle physics," *Monthly Notices of the Royal Astronomical Society*, vol. 398, no. 4, pp. 1601–1614, Oct. 2009.

[29] Z. Rustamkulov, D. K. Sing, R. Liu, and A. Wang, "Analysis of a jwst nirspec lab time series: Characterizing systematics, recovering exoplanet transit spectroscopy, and constraining a noise floor," *The Astrophysical Journal Letters*, vol. 928, no. 1, p. L7, mar 2022. [Online]. Available: https://dx.doi.org/10.3847/2041-8213/ac5b6f

[30] K. Glidic, E. Schlawin, L. Wiser, Y. Zhou, D. Deming, and M. Line, "Atmospheric Characterization of Hot Jupiter CoRoT-1 b Using the Wide Field Camera 3 on the Hubble Space Telescope," *Astronomical Journal*, vol. 164, no. 1, p. 19, Jul. 2022.

[31] T. Bell, E.-M. Ahrer, J. Brande, A. Carter, A. Feinstein, G. Caloca, M. Mansfield, S. Zieba, C. Piaulet, B. Benneke, J. Filippazzo, E. May, P.-A. Roy, L. Kreidberg, and K. Stevenson, "Eureka!: An End-to-End Pipeline for JWST Time-Series Observations," *The Journal of Open Source Software*, vol. 7, no. 79, p. 4503, Nov. 2022.

[32] J. Kirk, M. López-Morales, P. J. Wheatley, I. C. Weaver, I. Skillen, T. Louden, J. McCormac, and N. Espinoza, "LRG-BEASTS: Transmission Spectroscopy and Retrieval Analysis of the Highly Inflated Saturn-mass Planet WASP-39b," *Astronomical Journal*, vol. 158, no. 4, p. 144, Oct. 2019.

[33] C. W. Ormel and M. Min, "ARCiS framework for exoplanet atmospheres. The cloud transport model," *Astronomy and Astrophysics*, vol. 622, p. A121, Feb. 2019.

[34] P. Irwin, N. Teanby, R. de Kok, L. Fletcher, C. Howett, C. Tsang, C. Wilson, S. Calcutt, C. Nixon, and P. Parrish, "The nemesis planetary atmosphere radiative transfer and retrieval tool," *Journal of Quantitative Spectroscopy and Radiative Transfer*, vol. 109, no. 6, pp. 1136–1150, 2008, spectroscopy and Radiative Transfer in Planetary Atmospheres. [Online]. Available: https://www.sciencedirect.com/science/article/pii/S0022407307003378

[35] M. R. Line, A. S. Wolf, X. Zhang, H. Knutson, J. A. Kammer, E. Ellison, P. Deroo, D. Crisp, and Y. L. Yung, "A Systematic Retrieval Analysis of Secondary Eclipse Spectra. I. A Comparison of Atmospheric Retrieval Techniques," *Astrophysical Journal*, vol. 775, no. 2, p. 137, Oct. 2013.

[36] P. E. Cubillos and J. Blecic, "The PYRAT BAY framework for exoplanet atmospheric modelling: a population study of Hubble/WFC3 transmission spectra," *Monthly Notices of the Royal Astronomical Society*, vol. 505, no. 2, pp. 2675–2702, Aug. 2021.

[37] J. W. Stock, D. Kitzmann, A. B. C. Patzer, and E. Sedlmayr, "FastChem: A computer program for efficient complex chemical equilibrium calculations in the neutral/ionized gas phase with applications to stellar and planetary atmospheres ," *Monthly Notices of the Royal Astronomical Society*, vol. 479, no. 1, pp. 865–874, 06 2018. [Online]. Available: https://doi.org/10.1093/mnras/sty1531

[38] T. Guillot, "On the radiative equilibrium of irradiated planetary atmospheres," *Astronomy and Astrophysics*, vol. 520, p. A27, Sep. 2010.

[39] T. O. Husser, S. Wende-von Berg, S. Dreizler, D. Homeier, A. Reiners, T. Barman, and P. H. Hauschildt, "A new extensive library of PHOENIX stellar atmospheres and synthetic spectra," *Astronomy and Astrophysics*, vol. 553, p. A6, May 2013.

[40] W. J. Handley, M. P. Hobson, and A. N. Lasenby, "POLYCHORD: next-generation nested sampling," *Monthly Notices of the Royal Astronomical Society*, vol. 453, no. 4, pp. 4384–4398, Nov. 2015.

[41] E. Higson, W. Handley, M. Hobson, and A. Lasenby, "Dynamic nested sampling: an improved algorithm for parameter estimation and evidence calculation," *Statistics and Computing*, vol. 29, no. 5, p. 891–913, Dec. 2018. [Online]. Available: http://dx.doi.org/10.1007/s11222-018-9844-0

[42] J. Tennyson, S. N. Yurchenko, A. F. Al-Refaie, E. J. Barton, K. L. Chubb, P. A. Coles, S. Diamantopoulou, M. N. Gorman, C. Hill, A. Z. Lam, L. Lodi, L. K. McKemmish, Y. Na, A. Owens, O. L. Polyansky, T. Rivlin, C. Sousa-Silva, D. S. Underwood, A. Yachmenev, and E. Zak, "The ExoMol database: Molecular line lists for exoplanet and other hot atmospheres," *Journal of Molecular Spectroscopy*, vol. 327, pp. 73–94, Sep. 2016.

[43] S. N. Yurchenko, A. F. Al-Refaie, and J. Tennyson, "EXOCROSS: a general program for generating spectra from molecular line lists," *Astronomy and Astrophysics*, vol. 614, p. A131, Jun. 2018.

[44] C. Hill, S. N. Yurchenko, and J. Tennyson, "Temperature-dependent molecular absorption cross sections for exoplanets and other atmospheres," *Icarus*, vol. 226, no. 2, pp. 1673–1677, 2013. [Online]. Available: https://www.sciencedirect.com/science/article/pii/S0019103512003041

[45] P. Mukherjee, D. Parkinson, and A. R. Liddle, "A Nested Sampling Algorithm for Cosmological Model Selection," *Astrophysical Journal Letters*, vol. 638, no. 2, pp. L51–L54, Feb. 2006.

[46] R. Trotta, "Bayes in the sky: Bayesian inference and model selection in cosmology," *Contemporary Physics*, vol. 49, no. 2, pp. 71–104, 2008. [Online]. Available: https://doi.org/10.1080/00107510802066753

[47] L. Mancini, M. Esposito, E. Covino, J. Southworth, K. Biazzo, I. Bruni, S. Ciceri, D. Evans, A. F. Lanza, E. Poretti, P. Sarkis, A. M. S. Smith, M. Brogi, L. Affer, S. Benatti, A. Bignamini, C. Boccato, A. S. Bonomo, F. Borsa, I. Carleo, R. Claudi, R. Cosentino, M. Damasso, S. Desidera, P. Giacobbe, E. González-Álvarez, R. Gratton, A. Harutyunyan, G. Leto, A. Maggio, L. Malavolta, J. Maldonado, A. Martinez-Fiorenzano, S. Masiero, G. Micela, E. Molinari, V. Nascimbeni, I. Pagano, M. Pedani, G. Piotto, M. Rainer, G. Scandariato, R. Smareglia, A. Sozzetti, G. Andreuzzi, and T. Henning, "The GAPS programme with HARPS-N at TNG. XVI. Measurement of the Rossiter-McLaughlin effect of transiting planetary systems HAT-P-3, HAT-P-12, HAT-P-22, WASP-39, and WASP-60," *Astronomy and Astrophysics*, vol. 613, p. A41, May 2018.

Acknowledgments

I thank my supervisor Dr. Tiziano Zingales for his support, patience, insight and comments during my work on this thesis, as well as for enabling me to use the **kraken** cluster at our department, which helped greatly with speeding up the atmospheric retrievals performed in this work.